A dysprosium quantum gas in highly controllable optical traps

Masterarbeit
vorgelegt von
Matthias Wenzel

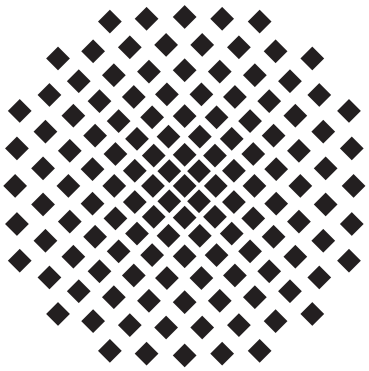

Hauptberichter: Prof. Dr. Tilman Pfau
Mitberichter: Prof. Dr. Martin Dressel

5. Physikalisches Institut, Universität Stuttgart
20. März 2015

Ehrenwörtliche Erklärung

Hiermit erkläre ich, dass ich diese Arbeit selbständig verfasst und keine anderen als die von mir angegebenen Hilfsmittel und Quellen verwendet habe. Alle wörtlich oder sinngemäß aus anderen Werken übernommenen Aussagen sind als solche gekennzeichnet. Die vorliegende Arbeit war weder Teil eines anderen Prüfungsverfahrens noch wurde sie bereits veröffentlicht. Weiterhin stimmt das elektronische Exemplar dieser Arbeit mit der gedruckten Version überein.

Stuttgart, den 20. März 2015

Matthias Wenzel

Abstract

In this thesis we present Bose-Einstein condensation of a gas of dysprosium atoms. Our cooling procedure relies on a Zeeman slower and a narrow-line magneto-optical trap. For better optical access we load the atoms directly in an optical dipole trap and transport them to a glass cell, where the atoms are loaded into a crossed optical trap. There we employ forced evaporative cooling towards condensation.
We measure the linewidth of the broad 421 nm transition to be $\Gamma_{421}/2\pi = (33 \pm 1)$ MHz. By measurements of the trap frequencies in the optical traps we derive the dynamic polarizability to (102±20) *a.u.* at $\lambda = 1070$ nm and (82±13) *a.u.* at 1064 nm. Additionally, we give an estimate of 10.5 *a.u.* at 532 nm.
We further employ a micrometer-resolution imaging system for in-trap imaging of the quantum gas. There we use phase-contrast imaging to nondestructively probe the latter. With the elctro-optical deflector system set up during this thesis the imaging system can be used to imprint tailored optical potentials.

Zusammenfassung

Inhalt dieser Arbeit ist die Erzeugung eines Bose-Einstein-Kondensats aus gasförmigen Dysprosiumatomen. Dysprosium zeichnet sich besonders durch sein hohes magnetisches Moment aus. Dies hat zur Folge, dass die langreichweitige dipolare Wechselwirkung der Atome stärker ist als die bekannte kurzreichweitige Kontaktwechselwirkung.
Um ein Dysprosium-Quantengas zu erhalten benutzen wir mehrere Kühlschritte, angefangen mit einem Zeeman-Abbremser. Dieser bremst die thermischen Atome so weit ab, dass sie von einer magneto-optischen Falle mit schmaler Linienbreite gefangen und weiter gekühlt werden können. Durch diese sind die Atome kalt genug um direkt in eine optische Dipolfalle geladen zu werden. In dieser werden die Atome zu einer Glaszelle transportiert. Nach dem Umladen in eine gekreuzte optische Falle und anschließender Verdampfungskühlung erhalten wir letztendlich ein Bose-Einstein Kondensat.
In dieser Arbeit wird die Linienbreite des 421 nm Übergangs zu $\Gamma_{421}/2\pi = (33 \pm 1)$ MHz bestimmt. Durch die Messung der Fallenfrequenzen in den verschiedenen optischen Fallen wird weiterhin die dynamische Polarisierbarkeit der Dysprosiumatome zu (102 ± 20) *a.u.* bei einer Wellenlänge von $\lambda = 1070$ nm und zu (82 ± 13) *a.u.* bei 1064 nm bestimmt. Desweiteren schätzen wir die Polarisierbarkeit bei 532 nm zu 10.5 *a.u.* ab.
Außerdem wird die Realisierung eines Abbildungssystems mit einer Auflösung von einem Mikrometer gezeigt. Das System mit einer Vergrößerung von 50 benutzen wir, um das Kondensat direkt in der Falle abzubilden. Ausserdem wurde während dieser Arbeit ein System von elektro-optischen Deflektoren geplant und aufgebaut. Dieses kann zusammen mit dem Abbildungssystem verwendet werden, um maßgeschneiderte Potentiale für die Untersuchung der langreichweitigen dipolaren Wechselwirkung zu erzeugen.

Contents

1. Introduction

Following the approach by Richard Feynman [1] research moves towards the simulation of complex quantum system by using simpler system with high controllability. Ultracold quantum gases are ideal model systems to study many-body phenomena known from solid state physics [2]. Compared to solid states these systems feature superior control of the external degrees of freedom, like the trapping potential, and internal properties, like the contact interaction in the vicinity of a Feshbach resonance [3].
Since the first observation of Bose-Einstein condensation [4–6] alkali atoms and the dominant contact interaction have been studied extensively. This contact interaction is isotropic and has a short-range character. Its strength is defined by a single parameter, the s-wave scattering length a. The latter can be tuned over several orders of magnitude [3] allowing to study, e.g. strongly interacting Fermi gases occurring in neutron stars [7].
One of the major achievements is the simulation of the quantum Ising model and the observation of an effective anti-ferromagnetic order in a tilted optical lattice [8]. Astonishingly, neutral atoms can also be used to simulate systems of charged particles by implementing artificial gauge fields [9]. However, as the interaction is still short range such systems show only effective long-range interactions mediated by e.g. the on-site interaction in optical lattices.
In contrast the magnetic dipole-dipole interaction, called *dipolar interaction* in this thesis, is anisotropic and long range [10]. With the long-range character real next-neighbor interactions become possible removing the restriction to on-site interactions. For bosonic quantum gases this opens the door to new quantum phenomena including supersolid and checkerboard phases [11, 12] which may serve as quantum memories [13]. For dipolar Fermi gases highly correlated states such as quantum Hall states have been predicted [14–16]. In two-component Fermi gases new ferromagnetic quantum phases with spatial anisotropy, called ferronematic phases, are expected [17, 18]. A first realization is the Hubbard model, where antiferromagnetic states are encountered [19].
Experimentally, studies of the dipolar interaction started with the Bose-Einstein condensation of chromium in 2005 [20]. Although the dipolar interaction is weak compared to the contact interaction in chromium [21] strong dipolar effects could be observed [22–24]. For these experiments the contact interaction was decreased in the vicinity of a Feshbach resonance in order to enter the strongly dipolar regime [25].
More recently, the focus shifted towards lanthanide atoms with larger magnetic moment and mass increasing the dipolar interaction. After the realization of ultracold Bose and Fermi gases in dysprosium [26–28] and erbium [29, 30] it becomes evident that these systems are well-suited for the investigation of dipolar effects. A unique consequence of

the strong dipolar interaction is the finite cross section for elastic collisions. It follows a universal scaling law depending only on the dipolar length a_{dd} and has been successfully used to cool identical fermions to quantum degeneracy [30].

Dysprosium

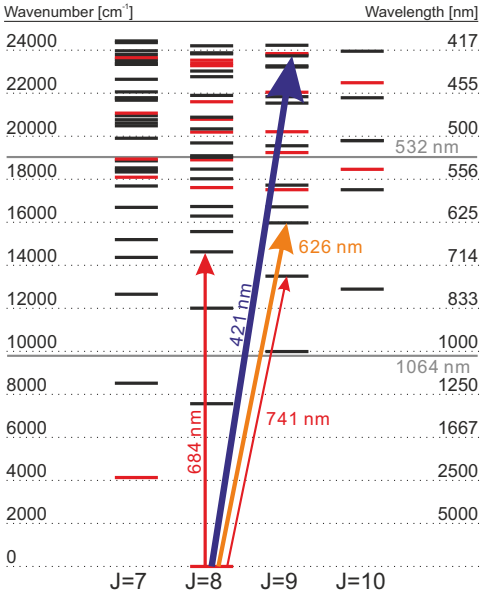

Figure 1.1.: Dysprosium energy levels and transitions used in experiments. Gray bars indicate wavelengths used for optical trapping at 532 nm and 1064 nm.

Dysprosium is a lanthanide element with 66 protons and electrons. Among the many isotopes there are two stable bosons ^{162}Dy (26 %) and ^{164}Dy (28 %) as well as two fermionic ones ^{161}Dy (19 %) and ^{163}Dy (25 %) with high natural abundance [31]. The electronic ground state $4f^{10}6s^2$ features an open 4f shell inside the closed 6s shell. With an orbital angular momentum $L = 6$ and a total electronic spin $S = 2$ the total angular momentum is $J = 8$ corresponding to a $^5I_8$ state. In contrast to the bosonic isotopes the fermions additionally have a finite nuclear spin of $I = 5/2$. The coupling to the total angular momentum J gives rise to a rich hyperfine structure characterized by quantum numbers $F = 11/2$ to $21/2$.
Because of the large total angular momentum, dysprosium (besides terbium) is the most magnetic stable element with a magnetic moment of 10 Bohr magneton. Thus the dipolar interaction becomes comparable in strength to the contact interaction, making dysprosium an ideal system to study dipolar effects.
Fig. 1.1 shows the energy levels along with the optical transitions used in dysprosium experiments. The $J = 8 \leftrightarrow 9$ cycling transitions are used for laser cooling purposes, e.g. for Zeeman slowing or magneto-optical trapping [31]. The $J = 8 \leftrightarrow 8$ transition at 684 nm can be used for optical pumping [32].

About this thesis

In chapter 2 we give an overview of the theoretical concepts used to describe Bose-Einstein condensation of an atom with both contact and dipolar interaction.
The following chapter focuses on optical dipole traps and the methods we use to detect the atoms. There we derive the framework needed to describe the trapping potentials created by the former. We also introduce an electro-optical deflector system, which is suited to create tailored optical potentials. In addition, we describe the detection methods, namely absorption and phase-contrast imaging, used in the experiment. We further show the first in-situ images acquired with our high-resolution imaging system.
We characterize the various cooling steps and the experimental procedure to create a dysprosium Bose-Einstein condensate in chapter 4. Additionally, we investigate the stability against a phonon-induced collapse of such a strongly dipolar condensate.

2. Dipolar Bose-Einstein condensates

In this chapter we develop the theoretical concepts to describe a dipolar Bose-Einstein condensate. The first section focuses on the non-interacting Bose gas and the associated phase transition. In the case of dysprosium we have two fundamentally different interactions between atoms. On the one hand the *contact interaction*, that we introduce in sec. 2.2, is isotropic and short-range. It is the dominant interaction in alkali atoms. On the other hand, there is the anisotropic and long-range *dipolar interaction*. Due to the high magnetic moment of dysprosium it is comparable in strength to the former, see sec. 2.3.

2.1. Phase transition to a BEC

As predicted by Satyendra Nath Bose and Albert Einstein in 1925 [33, 34] an ideal gas of bosons behaves differently compared to a classical gas of atoms described by Maxwell-Boltzmann statistics. In this case, the total number of particles $N_{\text{tot}} = \sum_i \langle N_i \rangle$ is given by the mean occupation number

$$\langle N_i \rangle = \frac{1}{\exp\left(\frac{E_i - \mu}{k_B T}\right) - 1} \tag{2.1}$$

of a state i with energy E_i according to the so-called *Bose-Einstein distribution* [35]. T denotes the equilibrium temperature of the sample, k_B the Boltzmann constant and μ the chemical potential. The latter is the energy needed to add or remove a particle of the system. In the classical limit for high temperatures $k_B T \gg (E_i - \mu)$ the Maxwell-Boltzmann distribution is retrieved. By decreasing the temperature the occupation number of lower energy states is increased. At a certain temperature T_c the quantum nature of the bosonic particles becomes important, allowing them to accumulate in the ground state of the system. This macroscopic population of the ground state is called a *Bose-Einstein condensate* (BEC). Dominated by the bosonic quantum statistics it allows us to study macroscopic quantum phenomena like superfluidity and the formation of vortices [36].
Experimentally, Bose-Einstein condensation was first discovered in dilute atomic gases of ^{87}Rb [4] and ^{23}Na [5] in 1995. In 2001 Eric A. Cornell, Wolfgang Ketterle and Carl E. Wieman were awarded the Nobel Prize in physics "for the achievement of Bose-Einstein condensation in dilute gases of alkali atoms, and for early fundamental studies of the

properties of the condensates". The books [35, 37] as well as review [38] give a more thorough introduction to the field and the particular phenomena.

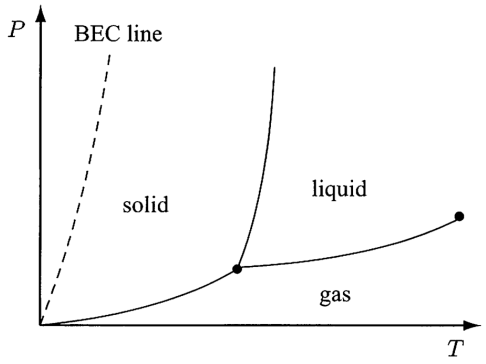

Figure 2.1.: Schematic P-T phase diagram. In equilibrium Bose-Einstein condensation occurs in the solid regime. Therefore the condensed phase of the gas is only metastable. Figure taken from [35].

As indicated by the phase diagram in fig. 2.1, a gaseous Bose-Einstein condensate is a metastable phase [35, chap. 9.1]. The dominating mechanism to bring the metastable phase into thermal equilibrium is molecule formation due to three-body recombination. Thus experiments work with dilute gases in a density regime of $n = 10^{13} - 10^{15}\,\mathrm{cm}^{-3}$, where three-body collision are rare. Therefore only two-body interactions are relevant for the description of a BEC. Yet, we focus on a non-interacting Bose gas first to obtain the critical temperature of the phase transition.
For an ideal Bose gas in a box with volume V the phase transition to a BEC is characterized by the phase space density

$$\mathcal{D} = n\lambda_{dB}^3 \tag{2.2}$$

with the density of particles $n = N_{\mathrm{tot}}/V$. λ_{dB} describes the thermal de Broglie wavelength

$$\lambda_{dB} = \sqrt{\frac{2\pi\hbar^2}{mk_BT}} \tag{2.3}$$

depending on the Boltzmann constant k_B, the atomic mass m and the temperature T. For a thermal gas the inter-particle spacing $n^{-1/3}$ is much larger than λ_{dB}. In this case the temperature is high and/or the density low, thus $\mathcal{D} \ll 1$. By decreasing the temperature and increasing the density the phase space density increases as well. At $\mathcal{D} = 1$ the inter-particle spacing is equal to the thermal de Broglie wavelength. For $\mathcal{D} > \zeta(3/2) \approx 2.612$ a macroscopic number of bosons populate the ground state[1]. This criterion allows us to define the critical temperature

$$k_BT_c^{\mathrm{free}} \equiv \frac{2\pi\hbar^2}{m}\left(\frac{n}{\zeta(3/2)}\right)^{2/3} . \tag{2.4}$$

[1] $\zeta(s)$ is the Riemann zeta function, defined as $\zeta(s) = \sum_{k=1}^{\infty} k^{-s}$.

As already mentioned the density is limited to the dilute regime where three-body losses are suppressed. Using eq. (2.4) we can thereby give a first estimate of the critical temperature $T_c^{\text{free}} \approx 1\,\mu\text{K}$ at a density of $n = 10^{14}\,\text{cm}^{-3}$.
Experimentally, atoms are in general trapped in harmonic potentials and thus do not have a uniform density distribution as assumed above. Thus we introduce an external trapping potential

$$V_{\text{ext}}(\mathbf{r}) = \frac{m}{2}\left(\omega_x^2 x^2 + \omega_y^2 y^2 + \omega_z^2 z^2\right) \tag{2.5}$$

depending on the trap frequencies ω_i. The underlying harmonic potential alters the density distribution and we obtain a critical temperature of

$$k_B T_c \equiv \hbar\bar{\omega}\left(\frac{N_{\text{tot}}}{\zeta(3)}\right)^{1/3} \approx 0.94\,\hbar\bar{\omega} N_{\text{tot}}^{1/3} \tag{2.6}$$

depending on $\bar{\omega} = (\omega_x\omega_y\omega_z)^{1/3}$, the geometric mean of the trap frequencies, and the total atom number N_{tot} [37, sec. 2.2]. Apparently the number of condensed atoms N, i.e. the atoms in the ground state, is an order parameter of the phase transition and given by the condensate fraction

$$\frac{N}{N_{\text{tot}}} = 1 - \left(\frac{T}{T_c}\right)^3 . \tag{2.7}$$

The wave function of a non-interacting BEC is the first eigenstate of a harmonic oscillator [37, sec. 2.3], which is described by a Gaussian function

$$\Psi(\mathbf{r}) = \sqrt{\frac{N}{\pi^{3/2} l_x l_y l_z}}\exp\left[-\frac{x^2}{2l_x^2} - \frac{y^2}{2l_y^2} - \frac{z^2}{2l_z^2}\right] \tag{2.8}$$

with widths $l_i = \sqrt{\hbar/(m\omega_i)}$. The atomic density is given by the squared wave function $n(\mathbf{r}) = |\Psi(\mathbf{r})|^2$. The geometric mean of the widths, the *harmonic oscillator length*,

$$a_{ho} = \sqrt{\frac{\hbar}{m\bar{\omega}}} \tag{2.9}$$

is a characteristic scale for the size of the condensate.
In the experiment, we typically obtain $N = 10^4$ condensed ^{164}Dy atoms at a mean trap frequency of $\bar{\omega} = 2\pi\cdot 100\,\text{Hz}$ with an oscillator length $a_{ho} = 0.8\,\mu\text{m}$ or $\approx 15\cdot 10^3$ Bohr radii. The total atom number of $N_{\text{tot}} = 8\cdot 10^4$ defines the critical temperature as $T_c \approx 190\,\text{nK}$.

2.2. Contact-interacting BEC

Furthermore, two-body interactions strongly influence the properties of a BEC. Here we introduce the contact interaction and derive the properties of a contact-interacting BEC. Two-body collisions in ultra-cold gases are dominated by a molecular potential. This molecular potential consists of an attractive van der Waals interaction ($\propto -r^{-6}$), which

is the interaction between two induced dipole moments. Combined with a repulsive contribution ($\propto r^{-12}$) due to electrostatic repulsion we obtain a short-range potential with a minimum at r_{VdW}, the characteristic interaction length [37, sec. 5.1]. Therefore we acquire bound states corresponding to the formation of a dimer. However, scattering of two particles with finite relative kinetic energy only introduces a phase shift of the wave function compared to the free-space wave function for $r \gg r_{\mathrm{VdW}}$ [39, sec. 10.5]. More precisely, for ultra-cold bosons only isotropic s-wave scattering ($l = 0$) is allowed because of an additional centrifugal barrier for higher relative orbital angular momentum number $l > 0$. Thus we can replace the complex molecular potential by an isotropic hard-sphere potential with radius a, which produces the same phase shift. Thereby we can describe the scattering process of two cold bosons by a single parameter, the *s-wave scattering length* a. The corresponding interaction potential is defined by

$$U_c(\mathbf{r}) \equiv g\,\delta(\mathbf{r}) \tag{2.10}$$

with Dirac delta function $\delta(\mathbf{r})$ and coupling strength

$$g \equiv \frac{4\pi\hbar^2}{m} a\,, \tag{2.11}$$

which is proportional to the previously described scattering length.

2.2.1. Gross-Pitaevskii equation

In the following, we apply the interaction potential U_c to our system with several thousands of atoms, each interacting with each other. We use a mean-field approach, that reduces this complex many-body problem to a one-body problem with an effective potential created by all other interacting particles. With this method we obtain the Hamiltonian

$$\begin{aligned} \hat{\mathrm{H}} &= \int \mathrm{d}\mathbf{r}\, \hat{\Psi}^\dagger(\mathbf{r},t) \left(-\frac{\hbar^2\nabla^2}{2m} + V_{\mathrm{ext}}(\mathbf{r}) \right) \hat{\Psi}(\mathbf{r},t) \\ &\quad + \frac{1}{2} \int \mathrm{d}\mathbf{r}\, \mathrm{d}\mathbf{r}'\, \hat{\Psi}^\dagger(\mathbf{r},t) \hat{\Psi}^\dagger(\mathbf{r}',t)\, U_c(\mathbf{r}-\mathbf{r}')\, \hat{\Psi}(\mathbf{r}',t) \hat{\Psi}(\mathbf{r},t) \end{aligned} \tag{2.12}$$

in second quantization. The first integral corresponds to the single particle kinetic and potential energies, while the second integral describes the mean-field energy due to interaction U_c. $\hat{\Psi}^\dagger(\mathbf{r},t)$ and $\hat{\Psi}(\mathbf{r},t)$ are the creation and annihilation operators for a particle at position $\mathbf{r}$. These satisfy the commutation relations

$$\left[\hat{\Psi}(\mathbf{r},t), \hat{\Psi}^\dagger(\mathbf{r}',t)\right] = \delta(\mathbf{r}-\mathbf{r}') \qquad \text{and} \qquad \left[\hat{\Psi}(\mathbf{r},t), \hat{\Psi}(\mathbf{r}',t)\right] = 0\,. \tag{2.13}$$

The field operator $\hat{\Psi}(\mathbf{r},t)$ in Heisenberg representation fulfills the relation

$$\begin{aligned} \mathrm{i}\hbar \frac{\partial}{\partial t} \hat{\Psi}(\mathbf{r},t) &= \left[\hat{\Psi}(\mathbf{r},t), \hat{\mathrm{H}}\right] \\ &= \left(-\frac{\hbar^2\nabla^2}{2m} + V_{\mathrm{ext}}(\mathbf{r}) + \int \mathrm{d}\mathbf{r}'\, \hat{\Psi}^\dagger(\mathbf{r}',t)\, U_c(\mathbf{r}-\mathbf{r}')\, \hat{\Psi}(\mathbf{r}',t) \right) \hat{\Psi}(\mathbf{r},t) \end{aligned} \tag{2.14}$$

leading us to the equations of motion [35, sec. 5.1]. For a large number of particles in a single state, the non-commutativity of the field operators becomes negligible and we can replace the field operator $\hat{\Psi}(\mathbf{r},t)$ by a classical field $\Psi(\mathbf{r},t)$. $\Psi(\mathbf{r},t)$ is called the order parameter or wave function of the condensate. Since this function varies slowly on distances of the molecular potential, we can substitute $\mathbf{r}' \to \mathbf{r}$. Thereby we arrive at the stationary *Gross-Pitaevskii equation* (GPE)

$$\mu\Psi(\mathbf{r}) = \left(-\frac{\hbar^2\nabla^2}{2m} + V_{\text{ext}}(\mathbf{r}) + g|\Psi(\mathbf{r})|^2\right)\Psi(\mathbf{r})\,, \tag{2.15}$$

which is a nonlinear differential equation and thus not analytically solvable. The chemical potential μ describes the energy needed to remove a particle from the sample. It corresponds to the energy per particle only in the non-interacting case.
Since this equation is not analytically solvable we introduce two approximations in the following sections, which allow to calculate some properties of an interacting condensate.

2.2.2. Thomas-Fermi approximation

The kinetic energy term $\propto \nabla^2\Psi$ in eq. (2.15) corresponds to the curvature of the order parameter. For large repulsive condensates ($a > 0$) in the limit $\frac{Na}{a_{ho}} \gg 1$ this so-called quantum pressure term becomes negligible as Ψ becomes increasingly flat [38, sec. III.D]. Within the *Thomas-Fermi approximation* this term is neglected, reducing the stationary GPE in eq. (2.15) to a linear equation

$$\mu\Psi(\mathbf{r}) = \Big(V_{\text{ext}}(\mathbf{r}) + g|\Psi(\mathbf{r})|^2\Big)\Psi(\mathbf{r})\,. \tag{2.16}$$

Solving for the density $n = |\Psi(\mathbf{r},t)|^2$ we obtain a simple solution

$$n_{TF}(\mathbf{r}) = \frac{\mu - V_{\text{ext}}(\mathbf{r})}{g} \tag{2.17}$$

in the region where $\mu > V_{\text{ext}}$ and $n_{TF} = 0$ for $\mu \leq V_{\text{ext}}$. Thus the density distribution resembles the external potential, in the case of a harmonic one it is an inverted parabola. Thus we arrive at

$$n_{TF}(\mathbf{r}) = n_0 \max\left[1 - \frac{x^2}{R_x^2} - \frac{y^2}{R_y^2} - \frac{z^2}{R_z^2}, 0\right] \tag{2.18}$$

with the Thomas-Fermi radii

$$R_i = \sqrt{\frac{2\mu}{m\omega_i}} \tag{2.19}$$

defined by the condition $\mu = V_{\text{ext}}(R_x, R_y, R_z)$ corresponding to the cloud boundary [37, sec. 6.2.2]. With fixed normalization $N = \int \mathrm{d}\mathbf{r}\,|\Psi(\mathbf{r})|^2$ we obtain the central density $n_0 = \mu/g$ and thereby the chemical potential

$$\mu = \frac{\hbar\bar{\omega}}{2}\left(\frac{15Na}{a_{ho}}\right)^{2/5}\,, \tag{2.20}$$

which is large compared to the harmonic oscillator spacing $\hbar\bar{\omega}$ for $\frac{Na}{a_{ho}} \gg 1$.
With the experimental values given in the last section we get $\frac{Na}{a_{ho}} \approx 60 \gg 1$ allowing us to utilize this much easier description. The spatial extend of the cloud is defined by the mean Thomas-Fermi radius $\bar{R} = (R_x R_y R_z)^{1/3} \approx 3.9\, a_{ho} = 5\,\mu\text{m}$. Thus the cloud size is increased by the repulsive interaction.

2.2.3. Gaussian approximation

So far we have assumed a repulsive interaction ($a > 0$), which stabilizes the condensate through the interaction potential. In the opposite case of an attractive interaction ($a < 0$) the central density of the cloud is increased and the condensate collapses for large atom numbers [38, sec. III.C]. To get a better insight we derive the energy functional starting with the mean-field Hamiltonian in eq. (2.12). Following the simplifications to obtain the GPE in the previous section, we arrive at

$$E[\Psi] = \int \mathrm{d}^3\mathbf{r} \left(\frac{\hbar^2}{2m} |\nabla\Psi|^2 + V_{\text{ext}} |\Psi|^2 + \frac{g}{2} |\Psi|^4 \right) . \tag{2.21}$$

with the first term corresponding to the quantum pressure, the second one for the external harmonic potential and a negative interaction term ($g < 0$) [37, sec. 6.1]. The parameter $N|a|/a_{ho}$ describes the strength of the interaction term compared to the quantum pressure and external potential. As argued in the previous section, the interaction term dominates for large atom numbers. Thus there is no minimum of the energy and therefore no stable solution of the GPE for $N|a|/a_{ho} \gg 1$. Yet in the intermediate regime $N|a| \approx a_{ho}$ the positive quantum pressure term counteracts the negative interaction term and a local minimum corresponding to a metastable solution of the GPE exists up to a certain critical atom number N_c. To determine N_c we use an isotropic ansatz

$$\Psi(r) = \sqrt{\frac{N}{\pi^{3/2}\sigma^3 a_{ho}^3}} \exp\left[-\frac{r^2}{2\sigma^2 a_{ho}^2} \right] \tag{2.22}$$

similar to the harmonic oscillator ground state of eq. (2.8) as a trial function [10, sec. 5.3]. The widths l_i are rewritten in terms of the dimensionless width $\sigma = l_i/a_{ho}$ assuming an isotropic trap. Fig. 2.2 shows the energy per particle over the width for different values of $N|a|/a_{ho}$. By inserting eq. (2.22) in the energy functional and solving for a minimum we can determine the critical atom number $N_{\text{crit}} \approx 0.671\, a_{ho}/|a|$ [38, sec. III.C].
Experimentally, some atomic elements have negative scattering length, e.g. ^{7}Li with $a = -25\, a_0$ [3], and thus condensate atom numbers are limited. In the first ^{7}Li BEC up to 1300 condensed atoms were observed, which is comparable to $N_{\text{crit}} \approx 1600$ calculated with the approach presented here [40].
In contrast, Bose-Einstein condensation of ^{162}Dy and ^{164}Dy [26, 28] indicates that the scattering length is positive for both isotopes. Therefore BECs are stable considering

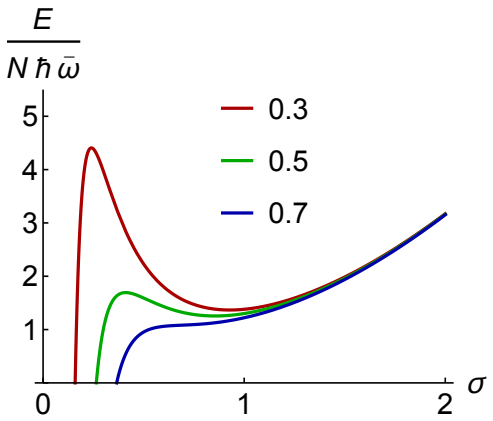

Figure 2.2.: Energy per particle E/N in units of $\hbar\bar{\omega}$ over dimensionless width σ of the Gaussian in eq. (2.22). Curves show different values of $N|a|/a_{ho}$ with the local minimum disappearing for a value of 0.671.

the contact interaction. However, dysprosium features a non-negligible dipolar interaction which can destabilize the condensate for certain trap geometries as described in the following section.

2.3. Dipolar interactions in BECs

The outstanding property of dysprosium is its high magnetic moment of $\mu_m = 10\,\mu_B$. The magnetic moment gives rise to a strong dipole-dipole interaction with a strength comparable to the contact interaction introduced in the previous section. Here, we introduce the *dipole-dipole interaction* (DDI) and derive a criterion for the stability of a dipolar BEC. The DDI also influences the critical temperature for condensation [41, 42] and other properties of the condensate.

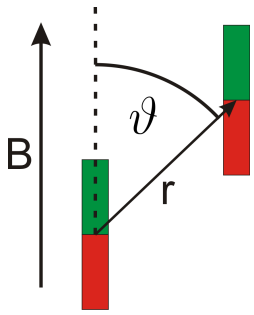

Figure 2.3.: Schematic of two interacting magnetic dipoles oriented parallel to the magnetic field **B**. These are separated by a distance r under an angle ϑ to the magnetic field axis. In a head-to-tail configuration ($\vartheta = 0°$) the interaction is attractive, while it is repulsive in a side-by-side configuration ($\vartheta = 90°$). Figure taken from [43].

The interaction potential for two magnetic dipoles with magnetic moment μ_m is given by

$$U_{dd}(\mathbf{r}) = \frac{\mu_0 \mu_m^2}{4\pi} \frac{1 - 3\cos^2 \vartheta}{r^3} \tag{2.23}$$

and depends on the vacuum permeability μ_0 as well as the distance r between atoms and the relative angle ϑ to the polarization axis [10, sec. 2.1]. The latter is defined by the magnetic field $\mathbf{B}$, as illustrated in fig. 2.3. The interaction scales as r^{-3} and is thus a long-range interaction in three dimensions. Therefore it cannot be replaced by a pseudo-potential as in the case of the contact-interaction [10, sec. 1.2]. The other remarkable feature is the anisotropy due to the dependence on the relative angle ϑ, which determines the sign of the interaction. Therefore we introduce the *magic angle* $\vartheta_0 = \arccos(1/\sqrt{3}) \approx 54.7°$ where the interaction term U_{dd} is zero. In a head-to-tail configuration of the dipoles ($\vartheta < \vartheta_0$) the dipolar interaction is attractive ($U_{dd} < 0$), while it is repulsive for a side-by-side configuration ($\vartheta > \vartheta_0$).
To compare the strength of dipolar and contact interaction we define the *dipolar length*

$$a_{dd} \equiv \frac{\mu_0 \mu_m^2 m}{12\pi\hbar^2} \tag{2.24}$$

similar to the s-wave scattering length a. The relative dipolar strength

$$\varepsilon_{dd} \equiv \frac{a_{dd}}{a} = \frac{\mu_0 \mu_m^2 m}{12\pi\hbar^2 a} \tag{2.25}$$

is given by the ratio of the two lengths. The coefficients in eq. (2.24) are chosen in a way that for $\varepsilon_{dd} \geq 1$ a homogenous condensate is unstable [10, sec. 3].
For alkali atoms with one electron in an s-shell and thus a magnetic moment of $1\,\mu_B$ the relative strength is $\varepsilon_{dd} \ll 1$. E.g. for ^{87}Rb we get $\varepsilon_{dd} = 0.007$. Therefore the dipolar interaction is usually negligible in alkali atoms. The first dipolar condensates were observed with ^{52}Cr in our group [20, 44]. It features a larger magnetic moment of $6\,\mu_B$ yielding a significant relative strength of $\varepsilon_{dd} = 0.16$. Here a Feshbach resonance [3] was used to lower the scattering length a and thus increase ε_{dd} to enter the strongly dipolar regime [25]. The downside are increased atom losses due to three-body recombination close to a Feshbach resonance, which practically limits the lifetime in experiments.
More recently lanthanides with larger mass and larger magnetic moment have been investigated. One of these is ^{168}Er with a magnetic moment of $7\,\mu_B$ and a relative dipolar strength $\varepsilon_{dd} = 0.33 - 0.44$, calculated for a background scattering length $a = 150 - 200\,a_0$ [29]. With comparable mass and a magnetic moment of $10\,\mu_B$ the relative dipolar strength is larger in dysprosium. For ^{164}Dy we obtain $\varepsilon_{dd} = 1.33$, which promises strong dipolar effects. The s-wave scattering length a of dysprosium is unknown up to now, thus we assume $a \approx 100\,a_0$ as in the case of ^{87}Rb or ^{52}Cr [3].

2.3.1. Long-range anisotropic dipolar interaction

Following the approach in sec. 2.2.1 we also want to extend the Gross-Pitaevskii equation eq. (2.15) with the dipolar interaction in eq. (2.23). Thus we use the mean-field approach

to get an effective dipolar interaction

$$\Phi_{dd}(\mathbf{r}) = \int \mathrm{d}^3\mathbf{r}' \, |\Psi(\mathbf{r},t)|^2 \, U_{dd}(\mathbf{r}-\mathbf{r}') \, . \tag{2.26}$$

In contrast to the van der Waals interaction, the dipolar interaction is long-range and thus we cannot replace it by a simpler contact-like potential [10, sec. 2.1]. This leads us to the modified non-local GPE

$$\mathrm{i}\hbar \frac{\partial}{\partial t}\Psi(\mathbf{r},t) = \left(-\frac{\hbar^2\nabla^2}{2m} + V_{\mathrm{ext}}(\mathbf{r}) + g|\Psi(\mathbf{r},t)|^2 + \Phi_{dd}(\mathbf{r}) \right) \Psi(\mathbf{r},t) \tag{2.27}$$

with the dipolar mean-field interaction term Φ_{dd}.
To illustrate the behavior of this interaction term we recall the density distribution

$$n_{TF}(\mathbf{r}) = n_0 \max\left[1 - \frac{r^2}{\bar{R}^2}, 0 \right] \tag{2.28}$$

of a contact-interacting BEC in the Thomas-Fermi limit, see eq. 2.18. For convenience we assume a spherically symmetric trap (Thomas-Fermi radius $\bar{R} = R_x = R_y = R_z$) and thus the density distribution is spherically symmetric as well. In this simplified case the interaction term

$$\Phi_{dd}(\mathbf{r}) = \frac{\varepsilon_{dd} m \bar{\omega}^2}{5} \left(1 - 3\cos^2\vartheta\right) \begin{cases} r^2 & \text{for } r \leq \bar{R} \\ \frac{\bar{R}^5}{r^3} & \text{for } r > \bar{R} \end{cases} \tag{2.29}$$

can be calculated in the perturbative regime $\varepsilon_{dd} \ll 1$ [10, sec. 2.1]. As shown in fig. 2.4 the interaction Φ_{dd} is attractive along the polarization axis and repulsive perpendicular to it. Thus it reproduces the interaction potential U_{dd} of two dipoles.
Therefore a spherical contact-interacting condensate becomes elongated along the magnetic field axis due to the dipolar interaction. Such a change of the cloud's shape due to internal magnetic forces is called the *magnetorestriction effect* [10].

2.3.2. Stability of a dipolar BEC

As seen in the previous section the dipolar interaction can be attractive and the strength of both dipolar and contact interaction is on the same order of magnitude in dysprosium, which can destabilize a strongly dipolar condensate even for a repulsive contact interaction. Here we show an approach to derive the stability based on the Gaussian approximation (sec. 2.2.3) for a BEC with contact and dipolar interaction.
Thus we extend the energy functional of eq. (2.21) by the dipolar interaction $\Phi_{dd}(\mathbf{r})$ defined in eq. (2.26) to get

$$E\left[\Psi\right] = \int \mathrm{d}^3\mathbf{r} \left(\frac{\hbar^2}{2m}|\nabla\Psi|^2 + V_{\mathrm{ext}}|\Psi|^2 + \frac{g}{2}|\Psi|^4 + \frac{1}{2}|\Psi|^2\Phi_{dd} \right) , \tag{2.30}$$

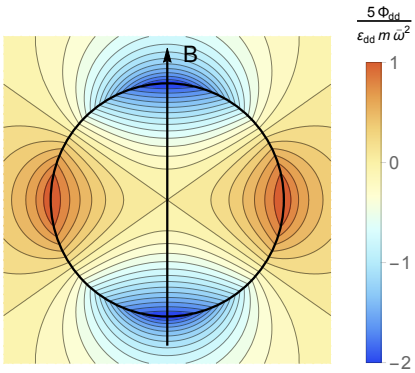

Figure 2.4.: Mean-field interaction term Φ_{dd} of eq. (2.29) for a spherical symmetric trap with Thomas-Fermi radius $\bar{R}$ (denoted by the black circle). The interaction term is negative (blue) and thus attractive at the edge of the cloud along the magnetic field axis B, while it is repulsive (red) perpendicular to it. The DDI breaks the spherical symmetry of the trap leading to an elongated condensate along the magnetic field.

as shown in [24]. As explained in sec. 2.2.3 regarding the stability of a contact-interacting BEC, we use a Gaussian trial function similar to the one in eq. (2.22). However, we assume a cylindrically symmetric trap with *trap aspect ratio* $\lambda \equiv \omega_z/\omega_r$. The two-body interaction term U_{dd} is cylindrically symmetric with respect to the polarizing magnetic field B. Therefore we choose B parallel to the z axis and use a cylindrically symmetric Gaussian ansatz

$$\Psi(r) = \sqrt{\frac{N}{\pi^{3/2}\sigma_r^2\sigma_z a_{ho}^3}}\, \exp\left[-\frac{1}{2a_{ho}^2}\left(\frac{r^2}{\sigma_r^2}+\frac{z^2}{\sigma_z^2}\right)\right] . \tag{2.31}$$

with dimensionless radial and axial widths σ_r and σ_z, respectively. We also define the *cloud aspect ratio* $\kappa \equiv \sigma_r/\sigma_z$. For a purely contact-interacting condensate λ is equivalent to κ. Yet the shape of the condensate and thus κ is altered by the dipolar interaction, as described in the previous section.
By inserting ansatz (2.31) into the energy functional of eq. (2.30) we obtain the energy

$$\tilde{E} \equiv \frac{E}{N\hbar\bar{\omega}} = \frac{1}{4}\left(\frac{2}{\sigma_r^2}+\frac{1}{\sigma_z^2}\right) + \frac{1}{4\lambda^{2/3}}\left(2\sigma_r^2+\lambda^2\sigma_z^2\right) + \frac{N a_{dd}}{\sqrt{2\pi}a_{ho}\sigma_r^2\sigma_z}\left(\frac{a}{a_{dd}} - f(\kappa)\right) \tag{2.32}$$

per particle and oscillator energy $\hbar\bar{\omega}$ [24]. The first term corresponds to the quantum pressure and the second term to the external potential. Additionally, the third term combines both contact and dipolar interaction, which both scale $\propto N$ in eq. (2.32). This term depends on a function

$$f(\kappa) = \frac{1+2\kappa^2}{1-\kappa^2} - \frac{3\,\kappa^2}{(1-\kappa^2)^{3/2}}\,\mathrm{artanh}\left(\sqrt{1-\kappa^2}\right) \tag{2.33}$$

decreasing monotonically from $f(0) = 1$ to $f(\infty) = -2$.
Similar to the stability criterion for the contact interaction in sec. 2.2.3 there exists a local minimum of the energy $\tilde{E}(\sigma_r, \sigma_z)$. We search for this minimum for a certain parameter Na for fixed trap aspect ratio λ, mean trap frequency $\bar{\omega}$ and dipolar length a_{dd}. Thus by fixing the atom number N we can numerically search for a critical s-wave scattering length a_{crit}, where the minimum vanishes for $a < a_{\text{crit}}$ and the dipolar condensate becomes unstable. Fig. (2.5) illustrates this procedure for ^{162}Dy in an isotropic trap with $\bar{\omega} = 2\pi \cdot 100\,\text{Hz}$ and 10^5 atoms. For these conditions we obtain $a_{\text{crit}} = 124.7\,a_0$.

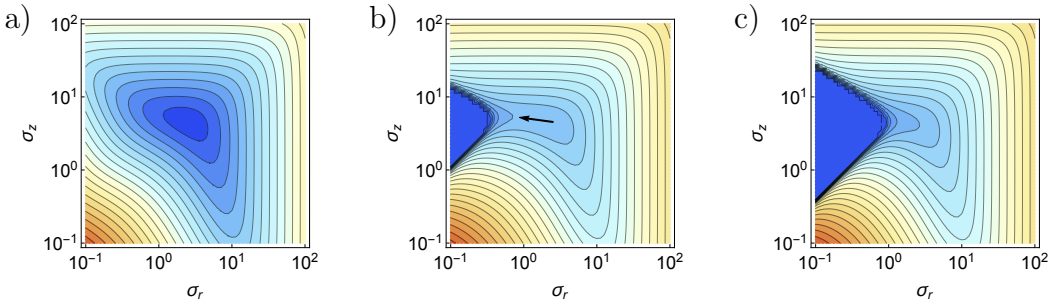

Figure 2.5.: Energy landscapes $\tilde{E}(\sigma_r, \sigma_z)$ for different scattering lengths a. There are $N = 10^5$ ^{162}Dy atoms ($a_{dd} = 131\,a_0$) in an isotropic trap ($\lambda = 1$) with $\bar{\omega} = 2\pi \cdot 100\,\text{Hz}$. For this configuration we obtain $a_{\text{crit}} = 124.7\,a_0$ numerically.
(**a**) With $a = 150\,a_0 > a_{\text{crit}}$ there exists a distinct local minimum at a cloud aspect ratio of $\kappa = \sigma_z/\sigma_r = 1.8$. (**b**) Close to a_{crit} for $a = 125\,a_0$ the condensate is radially compressed, thus increasing κ to 6.0 (indicated by arrow). (**c**) For $a = 100\,a_0$ there is no local minimum, because the condensate is not stable for $a < a_{\text{crit}}$.

Apparently, for the assumed s-wave scattering length of $a = 100\,a_0$ a dysprosium condensate is not stable under these conditions in an isotropic trap, see fig. (2.5c). However, we can determine the critical scattering length for various trap aspect ratios λ, as shown in fig. (2.6) for $N = 10^3$, 10^4 and 10^5 condensed atoms. The limiting cases for a_{crit} are $+a_{dd}$ and $-2\,a_{dd}$ as the parameter Na approaches ∞. From this calculation we can determine two important results. Firstly, a condensate of $N = 10^3$ atoms (red line) is stable ($a_{\text{crit}} < a$) for any trap aspect ratio λ. Secondly, in an oblate trap with $\lambda \geq 2$ (vertical line) a dysprosium condensate is stable for atom numbers up to $N = 10^5$.

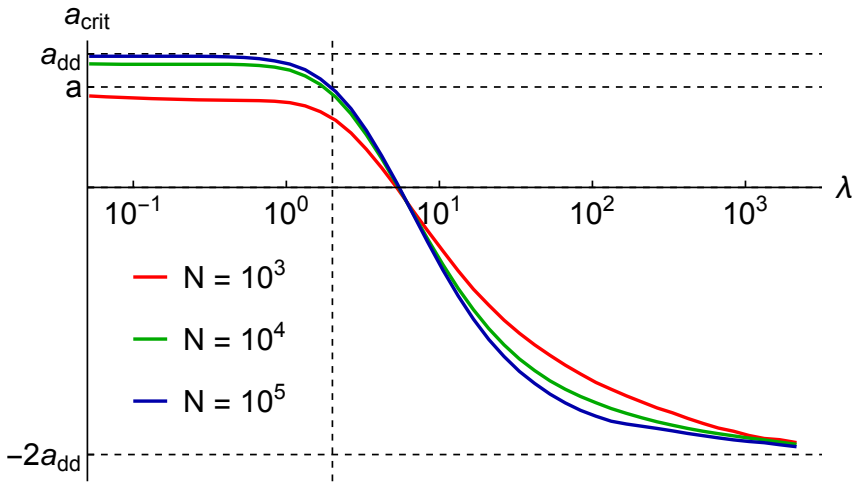

Figure 2.6.: Critical scattering length a_{crit} over trap aspect ratio $\lambda = \omega_z/\omega_r$ for a mean trap frequency $\bar{\omega} = 2\pi \cdot 100\,\text{Hz}$ and different atom numbers. In this case, a trap with $\lambda \geq 2$ is stable for any atom number assuming a scattering length of $a = 100\,a_0$. The upper and lower limits a_{dd} and $-2a_{dd}$ are shown as well.

3. Optical manipulation and detection of ultracold atoms

Methods for optical trapping and detection of neutral atoms are fundamental tools in ultracold atomic physics. Both techniques rely on atomic excitation and coherent light which is resonant or far-detuned with respect to these excitation energies. By having a strong control on the beam propagation and beam shape nearly arbitrary optical manipulation and high-resolution detection is possible. This chapter focuses on the experimental setup and techniques which are necessary for such a control.
Thus in the first section we develop the basics of optical trapping, so-called optical dipole traps (ODTs). There we derive the trapping potential for a crossed optical dipole trap. This indispensable tool is used to trap and evaporatively cool the atoms to quantum degeneracy. As seen in the previous chapter, for strongly dipolar condensates the aspect ratio of such a trap is important. The second section introduces an electro-optical deflector system (EOD). The creation of time-averaged potentials with a tightly focused ODT as well as preliminary design considerations and the optical setup are explained. To detect atoms we introduce two imaging methods in sec. 3.3, absorption and phase-contrast imaging. We use the latter for in-trap measurements combined with our high-resolution imaging setup, which is introduced in sec. 3.4. Additionally, we plan to use it to create the tightly focused trap for the creation of time-averaged potentials. Thus we focus on the resolution of this optical system for both imaging and trapping wavelengths.

3.1. Oscillator model of an optical dipole trap

The *dipole force* is used to optically trap neutral atoms. The following classical derivation is based on a review article by R. Grimm [45].
Placing an atom in an electric field $\mathbf{E}(t)$ distorts its charge distribution and therefore induces a dipole moment $\mathbf{p}(t) = \alpha\mathbf{E}(t)$ with a scalar complex polarizability α of the atom. The interaction energy V_{dip} of the induced dipole moment with the light field is extracted by averaging over the oscillating terms to obtain

$$V_{\mathrm{dip}}(\mathbf{r}) = -\frac{1}{2}\left\langle \mathbf{p}(t)\mathbf{E}(t)\right\rangle = -\frac{1}{2\varepsilon_0 c}\,\mathrm{Re}\{\alpha\}I(\mathbf{r})\,. \tag{3.1}$$

The intensity of the field is given by $I = 2\varepsilon_0 c|E|^2$ and the factor $1/2$ stems from the fact, that the dipole moment is induced. The depth of such a potential is proportional to the

light intensity I as well as the in-phase component $\mathrm{Re}\{\alpha\}$ of the polarizability. Being a conservative potential the dipole force simply is $F = -\nabla V_{\mathrm{dip}}$.
In addition, the absorbed power P_{abs} of the oscillator depends on the out-of-phase component of α. If we further treat the light field as a number of photons $\hbar\omega$ getting absorbed and spontaneously reemitted, the rate of such scattering events is given by

$$\Gamma_{\mathrm{sc}}(\mathbf{r}) = \frac{P_{\mathrm{abs}}}{\hbar\omega} = \frac{\langle \dot{\mathbf{p}}(t)\mathbf{E}(t)\rangle}{\hbar\omega} = \frac{1}{\hbar\varepsilon_0 c}\,\mathrm{Im}\{\alpha\} I(\mathbf{r})\,. \tag{3.2}$$

The interaction potential V_{dip} and the scattering rate Γ_{sc} characterize an optical dipole trap. The former directly gives the potential of captured atoms in such a trap and the latter is a quantity describing the heating of such an atomic sample. These equations hold for any classical neutral polarizable particle in an oscillating electric field and are solely dependent on the complex polarizability $\alpha(\omega)$ and the intensity distribution $I(\mathbf{r})$ of the light field.

Atomic polarizability

To obtain the polarizability $\alpha(\omega)$ we consider the Lorentz model of a classical oscillator. In this simple model, the electron with charge e and mass m_e is harmonically bound to the atom's nucleus with an eigenfrequency ω_0, called the optical transition frequency. Damping is due to dipole radiation of the oscillating electron and can be described by the Larmor formula

$$\Gamma_\omega = \frac{e^2\omega^2}{6\pi\varepsilon_0 m_e c^3}\,. \tag{3.3}$$

As already mentioned the oscillator is driven by an electric field $E(t)$ with oscillation frequency ω. Thereby we obtain the equation of motion

$$\ddot{x}(t) + \Gamma_\omega\,\dot{x}(t) + \omega_0^2\,x(t) = -\frac{e}{m_e}E(t)\,. \tag{3.4}$$

The displacement of the electron $r(t)$ is directly related to the dipole moment $p(t) = -ex(t) = \alpha E(t)$ and we can solve for the atomic polarizability

$$\alpha(\omega) = \frac{e^2}{m_e}\frac{1}{\omega_0^2 - \omega^2 - \mathrm{i}\omega\Gamma_\omega}\,. \tag{3.5}$$

Expressing this in terms of the resonant damping rate $\Gamma \equiv \Gamma_{\omega_0} = (\omega_0/\omega)^2\Gamma_\omega$ yields

$$\alpha(\omega) = 6\pi\varepsilon_0 c^3 \frac{\Gamma/\omega_0^2}{\omega_0^2 - \omega^2 - \mathrm{i}\omega^3\Gamma/\omega_0^2}\,. \tag{3.6}$$

This complex value can be expanded in terms of its real and imaginary part. It is further assumed that the detuning $\Delta \equiv \omega - \omega_0$ from resonance is large compared to the damping

rate Γ and we arrive[1] at

$$\begin{aligned}\alpha(\omega) &= 6\pi\varepsilon_0 c^3 \left[\frac{1}{2\omega_0^3}\left(\frac{\Gamma}{\omega_0-\omega}+\frac{\Gamma}{\omega_0+\omega}\right) - \mathrm{i}\,\frac{1}{4\omega_0^2}\left(\frac{\omega}{\omega_0}\right)^3\left(\frac{\Gamma}{\omega_0-\omega}+\frac{\Gamma}{\omega_0+\omega}\right)^2\right] \\ &= 6\pi\varepsilon_0 c^3 \left[-\frac{1}{2\omega_0^3}\left(\frac{\Gamma}{\Delta}\right) + \mathrm{i}\,\frac{1}{4\omega_0^2}\left(\frac{\Gamma}{\Delta}\right)^2\right] \end{aligned} \tag{3.7}$$

within the *rotating wave approximation* where the fast oscillating terms $(\omega_0+\omega)^{-1}$ are neglected, because ω and ω_0 are in the same order of magnitude and Δ^{-1} is much larger.

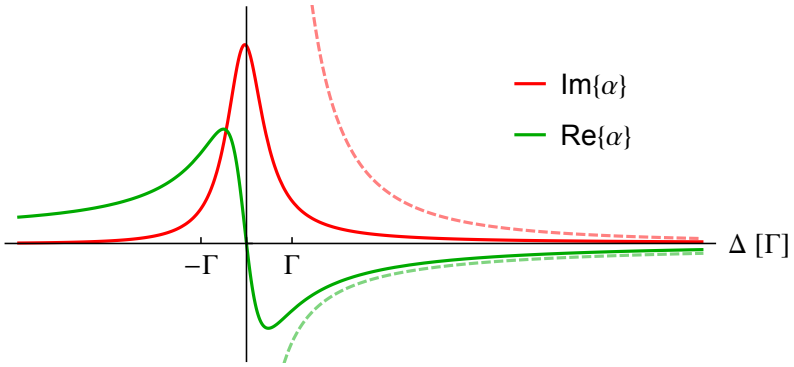

Figure 3.1.: Plot of the real and imaginary part of eq. (3.6) over detuning Δ. Γ is the full width at half maximum (FWHM) of $\mathrm{Im}\{\alpha\}$ and therefore the scattering rate. Dashed lines indicate the approximation for large detunings obtained in eq. (3.7).

The derived polarizability $\alpha(\omega)$ is valid in the regime $(\omega_0+\omega) \gg |\Delta| \gg \Gamma$ and we are able to apply it to eq. (3.1 & 3.2) to finally obtain

$$V_{\mathrm{dip}}(\mathbf{r}) = \frac{3\pi c^2}{2\omega_0^3}\left(\frac{\Gamma}{\Delta}\right) I(\mathbf{r}) \qquad \text{and} \qquad \Gamma_{\mathrm{sc}}(\mathbf{r}) = \frac{3\pi c^2}{2\hbar\omega_0^3}\left(\frac{\Gamma}{\Delta}\right)^2 I(\mathbf{r})\,. \tag{3.8}$$

Thus the potential is attractive if the driving light field is *red-detuned* ($\Delta < 0$) from resonance and atoms are drawn towards maximum intensity, while for a *blue-detuned* ($\Delta > 0$) field the potential becomes repulsive. Secondly, it becomes clear that the potential scales as I/Δ, while the scattering rate and therefore heating effects due to the light field scale as I/Δ^2.
So there are two possible methods to design an optical trap for neutral atoms. A far-red detuned trap created by a tightly focused laser beam is the much more common one. In order to have reasonable lifetimes of tens of seconds in such a trap the scattering rate needs to be negligible while still having a potential depth $V_{\mathrm{dip}} \gg k_B T$. Experimentally, these traps are operated at very high detunings (order of $10^6\,\Gamma$) and laser power (order

[1]The relations $\frac{1}{a-\mathrm{i}b} = \frac{a}{a^2+b^2} - \mathrm{i}\frac{b}{a^2+b^2} \approx \frac{1}{a} - \mathrm{i}\frac{b}{a^2}$ for $a \gg b$ and $\frac{1}{a^2-b^2} = \frac{1}{2a}\left(\frac{1}{a-b}+\frac{1}{a+b}\right)$ are used here.

of 1 W). The alternative involves a blue-detuned light pattern with zero intensity at the center usually involving a "doughnut" mode of the laser beam. The atoms get trapped at the intensity minimum and therefore the scattering rate is essentially zero. Yet it is not straight-forward to create such a mode and more laser power is needed to have the same potential depth, which is a disadvantage in most experimental realizations [45].
The derivation shown in this section is a fully classical treatment of a single optical transition. In a semi-classical approach of a two-level atom coupled to a classical light field the damping rate or spontaneous decay rate of the excited state is given by

$$\Gamma = \frac{\omega_0^3}{3\pi\varepsilon_0\hbar c^3} \left|\langle e|\mu|g\rangle\right|^2 \tag{3.9}$$

with the dipole matrix element between ground state $|g\rangle$ and excited state $|e\rangle$. In second order perturbation theory the *light shift* then is

$$\Delta V = \pm\frac{3\pi c^2}{2\omega_0^3}\frac{\Gamma}{\Delta} I \tag{3.10}$$

exactly corresponding to eq. (3.8) derived above [46]. This holds for low intensities or large detuning where saturation is negligible.
In principle, for real atoms with more than one optical transition the potential and scattering rate can be obtained by summing over the (Γ_i/Δ_i) terms for the respective optical transitions.

3.1.1. Focused beam traps

For the reasons stated above we use far-red detuned tightly focused laser beams to create the trapping potentials in the experiment. These are realized by focusing TEM_{00} Gaussian beams with a single lens. The intensity distributions $I(\mathbf{r})$ are shown below for a cylindrical symmetric Gaussian beam and two crossed elliptical beams.

Single beam trap

The radially symmetric intensity distribution

$$I(r,z) = \frac{2P}{\pi w(z)^2}\exp\left[-\frac{2r^2}{w(z)^2}\right] \tag{3.11}$$

of such a focused Gaussian beam has a Gaussian shape along the radial direction with an axial shape given by the e^{-2} beam radius

$$w(z) = w_0\sqrt{1+\left(\frac{z}{z_R}\right)^2}\,. \tag{3.12}$$

This beam is fully characterized by the power P and the minimum beam radius $w_0 = w(z = 0)$, called the *beam waist*. The characteristic length along the axial direction is the *Rayleigh length*

$$z_R = \frac{\pi w_0^2}{\lambda_L}, \tag{3.13}$$

where the beam radius increases to $w(z) = \sqrt{2}w_0$. $\lambda_L = 2\pi c/\omega$ is the laser wavelength. Figure 3.2 shows the relation between intensity and beam width.

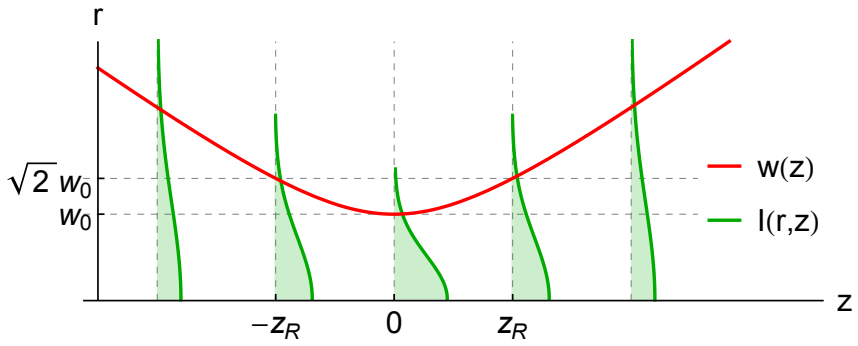

Figure 3.2.: Width $w(z)$ of a Gaussian beam (red) as defined in eq. (3.12). The radial intensity profiles $I(r, z)$ at certain z positions are shown in green. While the intensity is maximal at $r = z = 0$ the total beam power is conserved along z.

With the intensity distribution (3.11) at hand the trapping potential according to eq. (3.1) becomes

$$V_{\text{trap}}(r, z) = -\underbrace{\frac{\text{Re}\{\alpha\}P}{\varepsilon_0 \pi c w_0^2}}_{V_0} \frac{1}{1 + \left(\frac{z}{z_R}\right)^2} \exp\left[-\frac{2r^2}{w_0^2\left(1 + \left(\frac{z}{z_R}\right)^2\right)}\right] \tag{3.14}$$

with a certain trap depth $V_0 \equiv V_{\text{trap}}(0, 0)$ at the intensity maximum, usually on the order of 1 mK. For low temperatures $k_B T \ll V_0$, reachable with laser-cooled atoms, the atoms are confined close to the center of the trap allowing us to expand the potential

$$\begin{aligned} V_{\text{trap}}(r, z) &\approx -V_0\left[1 - 2\left(\frac{r}{w_0}\right)^2 - \left(\frac{z}{z_R}\right)^2\right] \\ &\equiv -V_0 + \frac{m}{2}\left(\omega_r^2 + \omega_z^2\right) \end{aligned} \tag{3.15}$$

and approximate it by a harmonic oscillator. This directly corresponds to the trapping potential in eq. (2.5) used to derive the characteristics of a BEC in chapter 2. With this simplification we can define a single oscillation frequency, the *trap frequency*,

$$\omega_\text{r} = \sqrt{\frac{4V_0}{m w_0^2}} \qquad \text{and} \qquad \omega_\text{z} = \sqrt{\frac{2V_0}{m z_R^2}} \overset{(3.13)}{=} \frac{\lambda_L}{\sqrt{2}\pi w_0}\,\omega_\text{r} \tag{3.16}$$

along the radial and axial direction, respectively. It is worth noting that the potential depth V_0 depends linearly on beam power P, while the trap frequencies ω_i scale as $\sqrt{P}$. In addition the trap frequencies set the time scale for collision events and therefore e.g. the thermal relaxation rate. With $\lambda_L \ll w_0$ the axial trapping frequency ω_z of a single focused Gaussian beam is much lower compared to the radial one.

Crossed beams

In order to ensure high local densities to increase the thermal relaxation rates for evaporative cooling (see sec. 4.2), we use a setup with two perpendicular crossed beams. The low axial trap frequency of one beam is then supported by the larger radial frequency of the other beam. The strong dipolar character of dysprosium requires an oblate trap in order to observe a stable condensate as shown in sec. 2.3.2. Therefore we use a set of two elliptical Gaussian beams, which intersect at their minimal waist position.

For such an elliptical beam eq. (3.11) is extended to two different beam radii $w_i(z)$ with waists $w_{0,i}$ along the x and y direction. For the k'th beam this leads to the non-radially symmetric intensity distribution

$$I_k(x,y,z) = \frac{2P_k}{\pi w_{x,k}(z) w_{y,k}(z)} \exp\left[-2\left(\frac{x^2}{w_{x,k}(z)^2} + \frac{y^2}{w_{y,k}(z)^2}\right)\right] \tag{3.17}$$

along the optical axis z. In the experiment we use one beam $I_1(y,z,x)$ pointing along the x direction and another beam $I_2(x,z,y)$ pointing along the y direction in lab coordinates[2]. Therefore the former is described by power P_1 and waists $w_{1,y}$, $w_{1,z}$, the latter by power P_2 and waists $w_{2,x}$, $w_{2,z}$. Due to the linear dependence on intensity the trapping potential then simply becomes

$$\begin{aligned} V_{\text{trap}}(x,y,z) &= -\frac{1}{2\varepsilon_0 c}\,\mathrm{Re}\{\alpha\}\big[I_1(y,z,x) + I_2(x,z,y)\big] \\ &\approx -\underbrace{\frac{\mathrm{Re}\{\alpha\}}{\varepsilon_0 \pi c}\left(\frac{P_1}{w_{1,y}w_{1,z}} + \frac{P_2}{w_{2,x}w_{2,z}}\right)}_{V_0} + \frac{m}{2}\left(\omega_x^2 + \omega_y^2 + \omega_z^2\right) \end{aligned} \tag{3.18}$$

within the harmonical approximation. Naturally the trap depth V_0 is given by both beam powers P_k as well as the respective waists. In this configuration the trap frequencies are

[2]Lab coordinates: z axis pointing in gravitational direction within a right-handed Cartesian coordinate system

defined as

$$\begin{aligned}
\omega_x &= \sqrt{\frac{\mathrm{Re}\{\alpha\}}{\varepsilon_0 \pi c m}} \sqrt{\frac{\lambda_L^2}{\pi^2} \frac{w_{1,y}^4 + w_{1,z}^4}{w_{1,y}^5 w_{1,z}^5} P_1 + \frac{4}{w_{2,x}^3 w_{2,z}} P_2} \overset{\lambda_L \ll w}{\approx} \sqrt{\frac{\mathrm{Re}\{\alpha\}}{\varepsilon_0 \pi c m}} \sqrt{\frac{4}{w_{2,x}^3 w_{2,z}} P_2} \\
\omega_y &= \sqrt{\frac{\mathrm{Re}\{\alpha\}}{\varepsilon_0 \pi c m}} \sqrt{\frac{4}{w_{1,y}^3 w_{1,z}} P_1 + \frac{\lambda_L^2}{\pi^2} \frac{w_{2,x}^4 + w_{2,z}^4}{w_{2,x}^5 w_{2,z}^5} P_2} \overset{\lambda_L \ll w}{\approx} \sqrt{\frac{\mathrm{Re}\{\alpha\}}{\varepsilon_0 \pi c m}} \sqrt{\frac{4}{w_{1,y}^3 w_{1,z}} P_1} \\
\omega_z &= \sqrt{\frac{\mathrm{Re}\{\alpha\}}{\varepsilon_0 \pi c m}} \sqrt{\frac{4}{w_{1,y} w_{1,z}^3} P_1 + \frac{4}{w_{2,x} w_{2,z}^3} P_2}
\end{aligned} \tag{3.19}$$

with the approximation for x and y that the axial confinement of a beam is weak compared to the radial one for similar beam parameters.
For theoretical calculations the three trap frequencies ω_x, ω_y and ω_z are the only parameters needed to model the harmonic trapping potential. For example, the phonon-induced collapse of a dipolar BEC depends on the *trap aspect ratio* $\lambda = \omega_z/\omega_r$ (see chapter 2). This is usually defined for a radially symmetric trap with radial and axial trap frequency ω_r and ω_z, respectively. In contrast to the definition in the previous section the symmetry axis z is defined by the direction of the magnetic field here. For non-radially symmetric traps we can define two trap aspect ratios $\lambda_{x,y} = \omega_z/\omega_{x,y}$ along the x and y axis.

3.2. Tailored potentials with electro-optical deflectors

Following proposals investigating the dipolar interaction in ring-shaped or multi-well potentials [47, 48], we plan to generate tailored time-averaged potentials in the experiment. The preliminary considerations and the crucial step of the generation of suitable intensity patterns with a scanning system is shown here as well as the optical setup to image these patterns on the atoms.

3.2.1. Time-averaged potentials

To create tailored potentials a red-detuned focused laser beam periodically scans a certain pattern with a cycle frequency f_{scan}. If this happens on a time scale much faster than the motion of the atom in the trap, defined by the trap frequency $\omega_{\mathrm{trap}} = 2\pi \cdot f_{\mathrm{trap}}$, the atom experiences a time-averaged potential

$$V_{\mathrm{trap}}(\mathbf{r}) \propto I_{\mathrm{trap}}(\mathbf{r}) = \langle I(\mathbf{r}, t) \rangle_{t_{\mathrm{scan}}} \, . \tag{3.20}$$

Angular brackets denote the time-average over one such cycle $t_{\mathrm{scan}} \equiv f_{\mathrm{scan}}^{-1}$. Obviously the potential depth $V_{\mathrm{trap}}(\mathbf{r})$ is proportional to the intensity $I(\mathbf{r}, t)$, as seen in eq. (3.1), as well as the accumulated rest time t_{rest} on a certain position $\mathbf{r}$. This section focuses on how to create such a tailored intensity pattern $I_{\mathrm{trap}}(\mathbf{r})$. The only constraint to a scanning laser

setup is $f_{\mathrm{scan}} \gg f_{\mathrm{trap}}$ in order to reduce parametric heating due to micromotion of the atoms [49].

Scanning systems based on acousto-optic deflectors (AODs) have been successfully used in atom optics experiments [49–51]. Technically, the diffraction angle in an AOD is proportional to the driving frequency. Therefore a deflection is due to a change in frequency and a rather complex frequency modulation is necessary to create tailored intensity patterns. In addition the diffraction efficiency also depends on the deflection angle.

In contrast to AODs the deflection angle of electro-optical deflectors (EODs) based on the Pockels effect is directly proportional to the applied voltage [52]. Thus the creation of more complex, non symmetric patterns is much more straight-forward. While in general the deflection angle and therefore the number of resolvable spots is lower, the response time is one order of magnitude faster [53]. EODs also feature higher and more uniform transmission efficiency as well as reduced pointing errors compared to AODs [54].

A completely different approach is the creation of static light patterns with spatial light modulators (SLMs). This holographic method relies on imprinting a phase with a liquid crystal display [55]. SLMs feature a larger number of resolvable spots and can be used to create arbitrary intensity patterns, even with helical wavefronts [56, 57]. The downside is the necessity for complex optimization algorithms, because the phase patterns are applied in Fourier space [58]. Another limitation is the low response time ($> 1\,\mathrm{ms}$). Both usually restrict the usage of SLMs to the static case.

3.2.2. Driving a scanning deflector system

In favor of higher flexibility and speed we use a scanning EOD system[3] consisting of two deflectors in orthogonal directions as well as a Pockels cell[4] to control the beam power. This setup is controlled by a real-time processing system[5] to have maximum flexibility & control.

The program of the latter is divided into two processes. A fast high-priority process subsequently stirs the beam to points $(x, y)_i$ with a certain rest time t_{rest} in between. The list of points is generated by a low-priority process with pre-defined functions to generate the patterns shown in fig. (3.3). This process running at 5 kHz also handles linear ramps, e. g. to move single dots in a multi-dot pattern or to carry out the transition between different patterns.

[3]Deflectors: 2× *Conoptics M311A* (1.5 mrad maximum deflection angle, 2.5 mm aperture, 90 % transmission at 532 nm) with a *Conoptics 412* (up to 200 kHz) dual amplifier.

[4]Pockels cell: *Conoptics M350-50C-01* (350:1 extinction ratio, 95 % transmission at 532 nm) with a *Conoptics 302RM* (up to 200 kHz) amplifier.

[5]System: *ADwin Gold II* programmed via *ADbasic* and linked to our experiment control with a *LabView* interface.

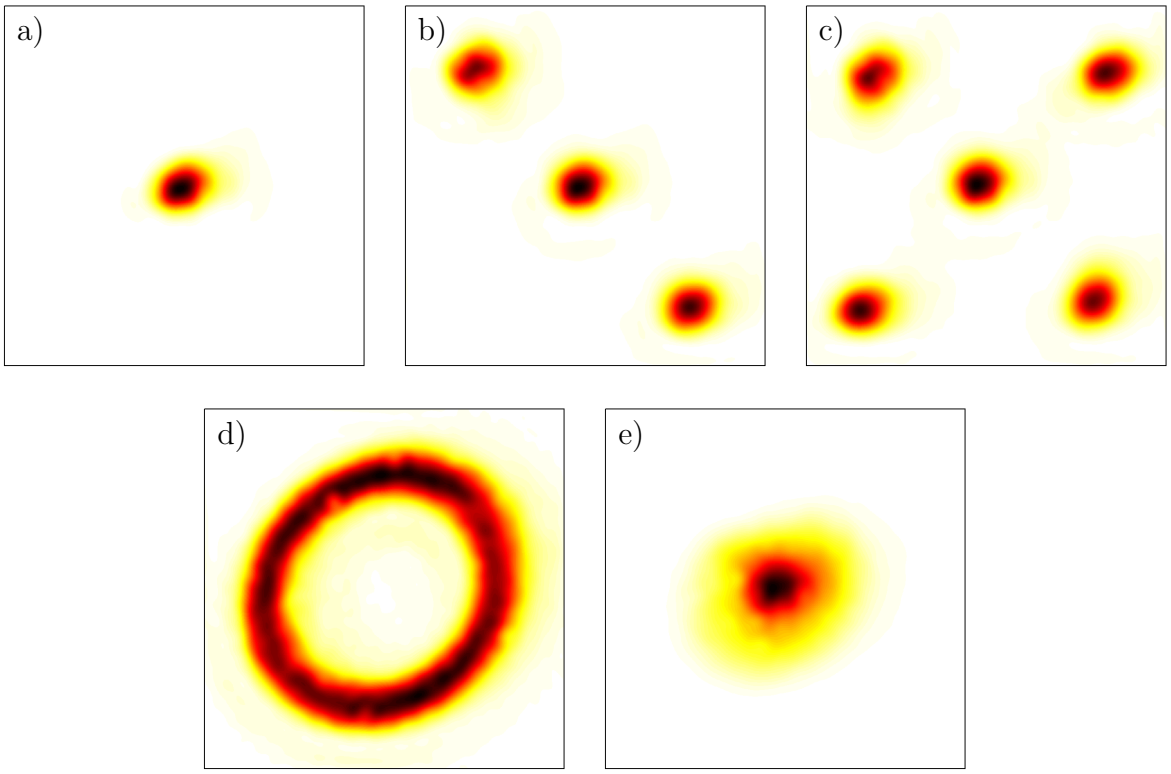

Figure 3.3.: Examples of different intensity patterns. The scan rate is 25 kHz. Images are taken after the deflector system with a CCD camera[6]. (**a**) Static image of the laser beam without being deflected. (**b**) & (**c**) Scanning patterns with multiple dots. With the optimized timing of the Pockels cell there is no blurring on the path between points. (**d**) A ring pattern created by placing 15 dots on a circle. In this case the pockels cell is always on to get a uniform intensity distribution along the ring. (**e**) Points are placed along an Archimedes spiral to increase the beam waist by a factor of 2.3 while aiming to preserve its Gaussian shape. This is useful to increase the trapping volume by a factor of $2.3^2 \approx 5.3$ during loading.

[6] An exposure time of 1 ms is chosen because the acquired intensity pattern then closely resembles the time-averaged potential with a trap frequency of roughly 1 kHz. Therefore possible fluctuations due to scanning of single dots should be the same in both cases and can be ruled out.
Camera model: *pco.pixelfly usb*

Timing aspects

In demand of a scan rate $f_{\text{scan}} \gg f_{\text{trap}} \approx 1\,\text{kHz}$ we investigated the timing of the components. For an exemplary scan rate of $f_{\text{scan}} = 60\,\text{kHz}$ the corresponding cycle time $t_{\text{scan}} \equiv f_{\text{scan}}^{-1} \approx 17\,\mu\text{s}$ is the time to scan the whole pattern. During this time the scanning system needs to move the beam to each dot (t_{EOD}) of a multi-well pattern and rest there for a certain time t_{rest}. The response time for a maximum change of the deflection angle between $+\alpha_0$ and $-\alpha_0$ is $t_{\text{EOD}} = 3.3\,\mu\text{s}$, while the Pockels cell's turn-on/off time is $t_{\text{PC}} = 1.5\,\mu\text{s}$. Both are limited by the capacitance of the electrodes around the optical crystals and the driving amplifiers. So, for a 3-dot pattern as shown in fig. (3.4a) there is $t_{\text{rest}} = (17\,\mu\text{s} - 3t_{\text{EOD}})/3 \approx 2.3\,\mu\text{s}$. With t_{rest} on the order of t_{EOD} the path between dots is blurred. To overcome this limitation we use the Pockels cell to turn off the beam while the deflectors move it. This is possible, because the Pockels cell is more than twice as fast as the deflectors. The optimal timing $t_{\text{off}} = 3.5\,\mu\text{s}$ was determined empirically in order to increase the dot-to-path intensity ratio, see fig. (3.4b). With $t_{\text{off}} > t_{\text{EOD}}$ the determined timing is valid for any number of dots. This also reveals that the maximum number of spots N_{s} is limited by f_{scan}. The rise time of the Pockels cell sets a lower limit for the rest time $t_{\text{rest}} = 1\,\mu\text{s}$. Therefore we get the relation

$$t_{\text{scan}} = N_s\,(t_{\text{EOD}} + t_{\text{rest}}) \quad \Leftrightarrow \quad N_{\text{s}} \cdot f_{\text{scan}} = (t_{\text{EOD}} + t_{\text{rest}})^{-1} \approx 230\,\text{kHz} \tag{3.21}$$

putting an upper limit to the number of distinctive spots at a certain scan rate. Also the incident light intensity on the deflector system needs to be a factor $t_{\text{scan}}/t_{\text{rest}}$ higher compared to a static non-deflected beam in order to reach the same intensity per dot. As mentioned before another constraint is $f_{\text{scan}} \gg f_{\text{trap}}$ limiting the number of spots to 9 at $f_{\text{scan}} = 25\,\text{kHz}$ in practice.

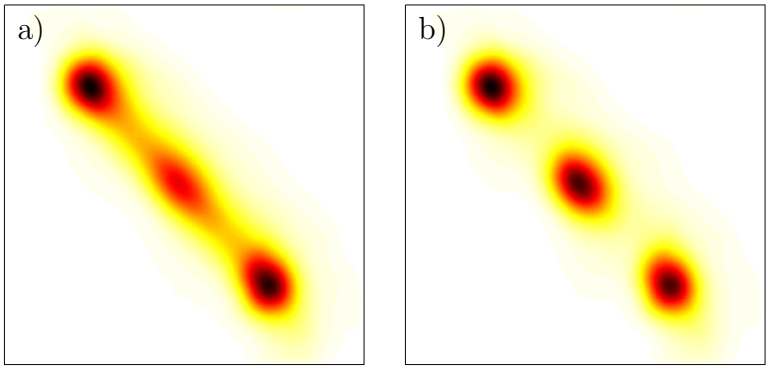

Figure 3.4.: A 3-dot pattern showing the effect of the pockels cell. Images are acquired the same way as in fig. (3.3). The scan rate is 60 kHz. (**a**) The dots are blurred without modulating the Pockels cell. (**b**) The Pockels cell is used to turn the scanning beam off for 3.5 μs inbetween the dots.

3.2.3. Beam propagation & optical setup for the EOD system

In order to imprint the generated patterns on a quantum gas with a size of several μm, we need an optical setup which is able to focus a single spot of such a pattern to a spot size on the order of 1 μm. As the minimal spot size is Abbe diffraction-limited, it will be always larger than $\lambda_L/2$. Therefore we operate this dipole trap at a wavelength of $\lambda_L = 532\,\text{nm}$. Compared to the other near-infrared dipole traps at 1064 or 1070 nm the diffraction-limited spot size is a factor of 2 smaller. However, the polarizability and thus the trap depth is an order of magnitude lower at similar intensities, see sec. 4.2.2.
In the following, we will use the maximum deflection angle of the EOD system to determine the effective deflection distance r_a and beam width w_a at the position of the atoms. For this the propagation of the deflected beam is described within ray transfer matrix analysis, also known as $ABCD$ matrix formalism (see e.g. [59]). Thereby the beam width $w(z)$ and distance $r(z)$ to the optical axis have to be treated separately. The former is modeled as a Gaussian beam, which is characterized by its initial beam waist $w_0 = 510\,\mu\text{m}$ at $z = 0$. In contrast its deflection given by the distance $r(z)$ to the undeflected optical axis is treated as a plane wave. It is characterized by $r(0) = 0$ and an initial deflection angle $\alpha_0 = 1.5\,\text{mrad}$ given by the maximum deflection angle of the deflector system.

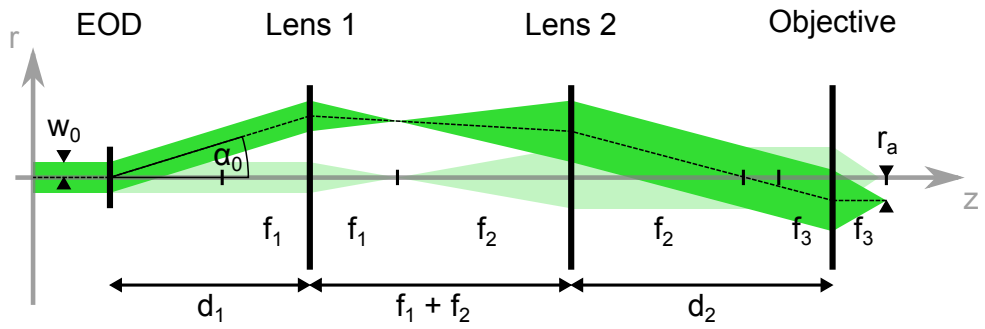

Figure 3.5.: Schematic of the deflector setup. An incident beam with waist w_0 is deflected in the EOD system by an angle α_0. The following telescope with focal lengths f_1 and f_2 magnifies the beam width by the factor $M = f_2/f_1$. Then the microscope objective (focal length f_3) focuses the beam on the atoms. The distance to the optical axis is called the deflection radius $r(z)$. The undeflected beam is indicated in light green.

As outlined in fig. 3.5, the setup consists of the deflector system (EOD) at $z = 0$ followed by two lenses with focal length f_1 and f_2 forming a telescope with magnification $M = f_2/f_1 = 750\,\text{mm}/100\,\text{mm} = 7.5$. Finally the essential part, a diffraction-limited microscope objective ($f_3 = 25.18\,\text{mm}$), is used to focus the deflected beam on the atom cloud. It is part of our high-resolution imaging setup, which is further described in sec. 3.4. Hence, we arrive at the corresponding ray transfer matrix

$$\mathrm{A_{EOD}} = \begin{pmatrix} 1 & d_1 \\ 0 & 1 \end{pmatrix} \begin{pmatrix} 1 & 0 \\ -\frac{1}{f_1} & 1 \end{pmatrix} \begin{pmatrix} 1 & f_1+f_2 \\ 0 & 1 \end{pmatrix} \begin{pmatrix} 1 & 0 \\ -\frac{1}{f_2} & 1 \end{pmatrix} \begin{pmatrix} 1 & d_2 \\ 0 & 1 \end{pmatrix} \begin{pmatrix} 1 & 0 \\ -\frac{1}{f_3} & 1 \end{pmatrix} \begin{pmatrix} 1 & f_3 \\ 0 & 1 \end{pmatrix} . \tag{3.22}$$

This simple treatment allows us to calculate the beam waist w_a and the deflection distance r_a at the position of the atoms as

$$w_a = \frac{f_3\,\lambda}{M\,\pi\,w_0} = 1.1\,\mu\text{m} \qquad \text{and} \qquad r_a = \frac{f_3\,\alpha_0}{M} = 5.0\,\mu\text{m}\,. \tag{3.23}$$

With these values at hand we can define the *resolution*

$$\eta(z) = \frac{r(z)}{w(z)} \tag{3.24}$$

as the number of distinctive spots with diameter $2\,w(z)$ over the full deflection range $2\,r(z)$. The resolution at the atoms

$$\eta_a = \frac{r_a}{w_a} = \frac{\pi\,w_0\,\alpha_0}{\lambda} = 4.5 \tag{3.25}$$

depends on initial beam waist w_0 and deflection angle α_0 which are both limited by the deflector system. The former is restricted by the EOD system's aperture size of 2.5 mm. The wavelength-dependence is due to the diffraction limit of the Gaussian beam. Thereby the maximum resolution is fixed by the deflector system and cannot be changed by the optical setup.
Additionally, the propagation for the deflected beam along the optical axis is shown in fig. 3.7a. We also implemented a second beam path, as shown in fig. 3.7b, where a telescope with $f_1 = 300\,\text{mm}$ and $f_2 = -75\,\text{mm}$ is used. This allows us to monitor the intensity patterns described in sec. 3.2 with the same resolution $\eta = 4.5$ and a spot size suitable for our CCD camera.
The full optical setup to create tailored potentials as well as the imaging path for high-resolution imaging are shown in fig. 3.8.

3.2.4. Expected potential depth of tailored structures

Assuming the derived beam waist $w_0 = 1.1\,\mu\text{m}$ of the trapping beam in the pervious section we can calculate the potential from eq. (3.14). The second ingredient is the real part of the polarizability, which we estimate experimentally to $\text{Re}\{\alpha\} \approx 10.5\,a.u.$ for a wavelength of 532 nm in sec. 4.2.2. Hence, we arrive at the trap depth

$$V_0 = \frac{\text{Re}\{\alpha\}P}{\epsilon_0 \pi c w_0^2} = -4.35\,\mu\text{K} \tag{3.26}$$

for a power $P = 3.5\,\text{mW}$ of a single non-deflected beam. In our setup the beam points along the gravitational axis z, so the weak axis of the beam is altered by the gravitational potential $V_g(z) = mgz$. The latter is defined by the atomic mass $m = 164\,\text{u}$ of ^{164}Dy and the gravitational acceleration $g = 9.81\,\frac{\text{m}}{\text{s}^2}$. Combining V_{trap} and V_g reduces the potential depth to $V_0' = -1.0\,\mu\text{K}$, see fig. 3.6. Such a trap is sufficiently deep to hold a BEC with

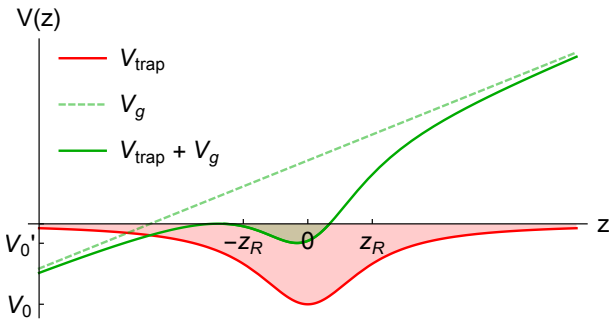

Figure 3.6.: Trapping potential (red) of a single focused laser beam along its propagation direction z. The gravitational potential $V_g(z) = mgz$ tilts the potential and reduces the potential depth from $V_0 = -4.35\,\mu$K to $V_0' = -1.0\,\mu$K. Offsets of the potentials are chosen to reflect the effective potential depth.

a transition temperature on the order of 100 nK. Furthermore we obtain the radial and axial trap frequencies $\omega_\mathrm{r} = 2\pi \cdot 4.3\,\mathrm{kHz}$ and $\omega_\mathrm{z} = 2\pi \cdot 430\,\mathrm{Hz}$ from eq. (3.16).
With the Gaussian ansatz introduced in sec. 2.3.2 we are also able to estimate the critical number N_crit of atoms. For atoms above N_crit the interaction destabilizes the condensate and it collapses. With the magnetic field and the beam in z direction, we get a prolate trap geometry with mean trap frequency $\bar{\omega} = (\omega_r^2\omega_z)^{1/3} = 2\pi \cdot 2.0\,\mathrm{kHz}$ and trap aspect ratio of $\lambda = \omega_z/\omega_r = 0.1$. Assuming a background scattering length $a = 100\,a_0$, we obtain a critical atom number of $N_\mathrm{crit} \approx 900$ with this method. Certainly this small number is due to the low trap aspect ratio caused by the single beam [24].
There is a simple approach to increase the trap aspect ratio in order to increase N_crit. We can use the underlying crossed ODT to hold the atoms against the gravitational potential. Therefore it is possible to work with less power in the deflected beam to only perturb the underlying potential. This approach was for example used in [49] with an underlying magnetic trap.

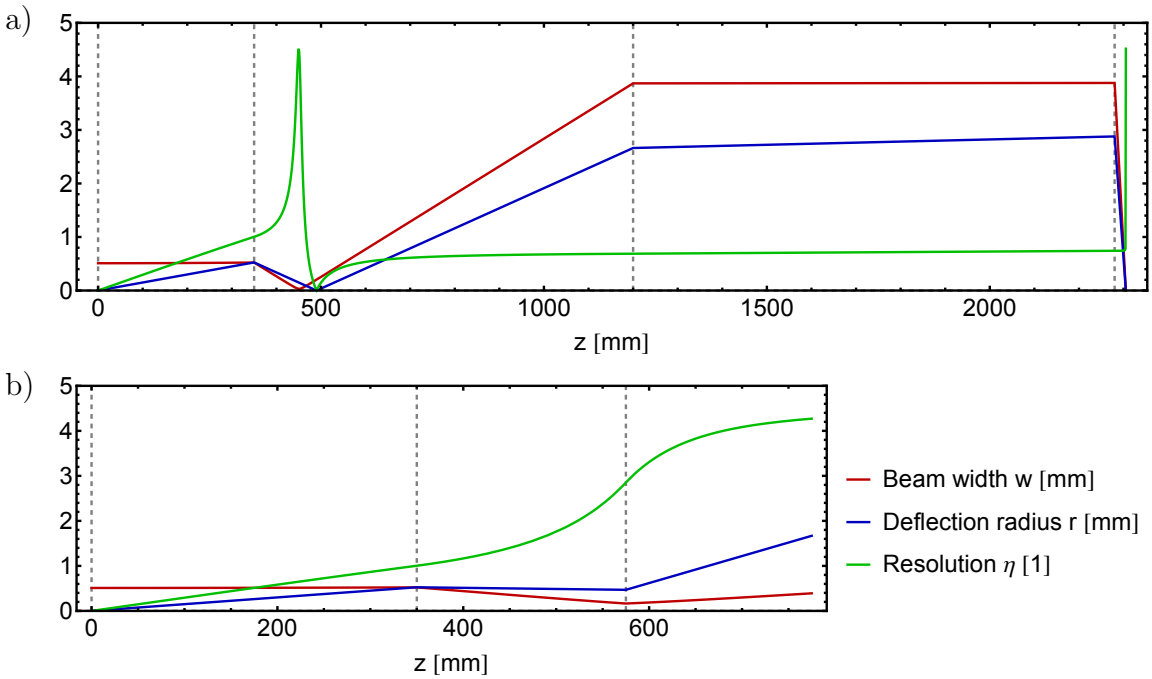

Figure 3.7.: Propagation of the beam width w, deflection radius r and resolution η along the optical axis z. The vertical lines denote the EOD system ($z = 0\,\text{mm}$), lens 1 & 2 as well as the microscope objective. (**a**) shows the path to the atoms with $f_1 = 100\,\text{mm}$, $f_2 = 750\,\text{mm}$ as well as $f_3 = 25.18\,\text{mm}$. In (**b**) the folding mirror is set to monitor the output of the EOD system after a $f_1 = 300\,\text{mm}$ and $f_2 = -75\,\text{mm}$ lens. Note that both paths have the same resolution $\eta_a = 4.5$ in the end.

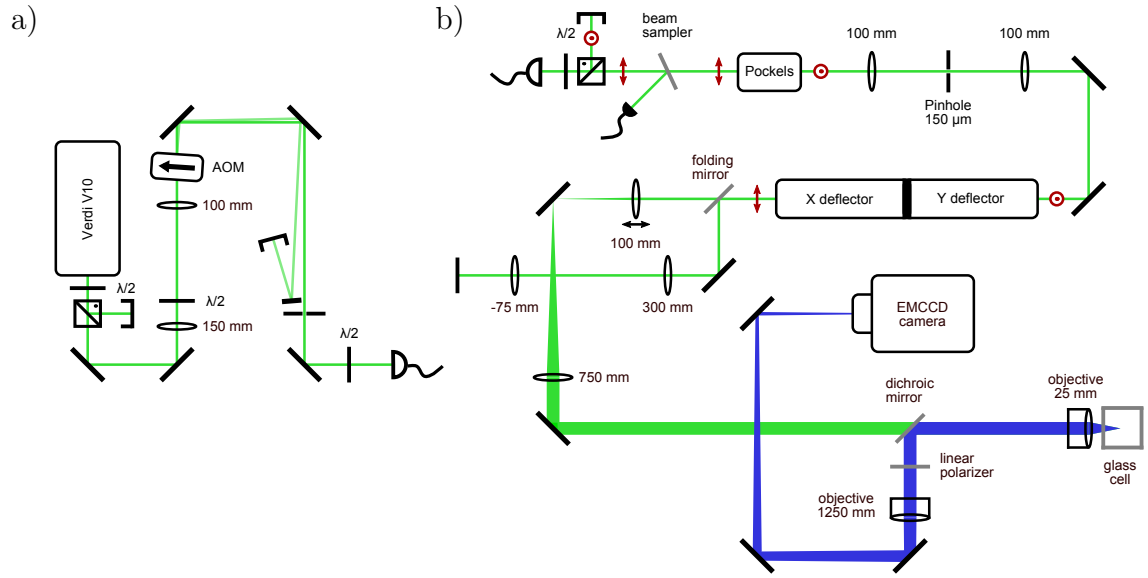

Figure 3.8.: Optical setup for the EOD system[7]. Green denotes the 532 nm trapping light and blue the 421 nm imaging path. (**a**) The laser output goes through an AOM to control the power of the beam and then into a high-power fiber. (**b**) Setup on the top level of the laser table. After the outcoupler a beam sampler reflects a small amount of light on a photo diode which is used with the AOM and a PI controller to stabilize the beam power. Up to 2 W are incident on the pockels cell that rotates the linear polarization by 90°. Subsequently a 1:1 telescope can be used in conjunction with an optional pinhole for mode cleaning of the beam. A 90° polarization rotator is placed between the two following EODs in order to deflect in both the x and y direction. The folding mirror can be used to monitor the EOD output on an EMCCD camera. On the path to the atoms the beam is magnified by a 7.5:1 telescope, transmitted through a dichroic mirror and then gets focused by the microscope objective into the glass cell. The image of the atoms (blue) is magnified by a factor of 50 and focused on a camera. The linear polarizer inbetween is crucial for phase-contrast imaging. Red denotes the polarization direction of the π-polarized trapping light.

[7]Components:
Laser *Coherent Verdi V10* (532 nm, running at 5 W), AOM *Neos 35085-3*, high-power coupler *OZ Optics HPUCO-8,A3HP-532-P-*AS*, high-power fiber *QPMJ-A3HPC,A3HPC-488-3.5/125-5AS-2-1*, beam sampler *Thorlabs BSF10-A*, photo diode *Thorlabs DET100A/M*, pockels cell *Conoptics M350-50*, deflectors *Conoptics 311A*, dichroic mirror *Thorlabs DMLP505L*, linear polarizer *Thorlabs WP25M-VIS*, EMCCD camera *Andor iXon3-897E-CSO-EXF*.

3.3. Imaging methods

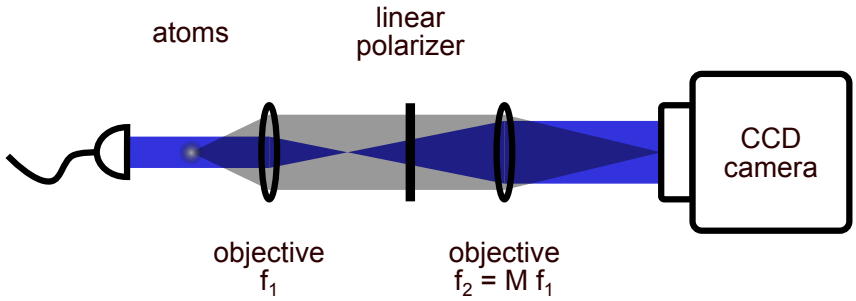

Figure 3.9.: Schematic imaging setup. A collimated beam (blue) is directed through the glass cell and the atom cloud. The two objectives magnify the effective image of the atoms (grey) by a factor M and focus it on a CCD camera. To switch from absorption imaging to phase-contrast imaging we place a linear polarizer in the beam path as described below.

Measuring the density distribution of a sample of atoms is a vital part of a quantum gas experiment. With the methods shown here quantities like the atom number and temperature can be extracted. The usual setup to probe the density distribution of a cloud of atoms is shown in fig. 3.9. The atoms are exposed to a probe laser which is then magnified by a telescope and imaged on a CCD camera. Apparently the density distribution $n(x, y, z)$ is integrated along the optical axis z of the beam allowing only to detect the column density

$$\tilde{n}(x, y) = \int n(x, y, z')\mathrm{d}z' \tag{3.27}$$

of the sample. A cloud of atoms with frequency-dependent polarizability $\alpha(\omega)$ and column density $\tilde{n}(x, y)$ alters the electric field of a probe beam by [40]

$$\frac{\mathrm{d}E}{\mathrm{d}z} = \mathrm{i}\varphi E \quad \Rightarrow \quad E = E_0\, e^{\mathrm{i}\varphi}\,. \tag{3.28}$$

In eq. (3.28) we introduced the complex phase

$$\varphi(\omega) = \frac{\omega}{2\varepsilon_0 c}\tilde{n}(x, y)\alpha(\omega) = \underbrace{\mathrm{Re}\{\varphi\}}_{\beta} + \mathrm{i}\underbrace{\mathrm{Im}\{\varphi\}}_{OD/2}, \tag{3.29}$$

which is proportional to the column density as well as the polarizability. Since the phase is complex, we can describe its real and complex part. As already shown in section 3.1 the polarizability shows a dispersive relation when approaching an atomic resonance $\omega = \omega_0$. Close to resonance the imaginary part dominates, while far off-resonant the real part dominates. With this knowledge, we introduce two possible imaging methods: Absorption imaging on resonance characterized by OD, the *optical density*, as well as phase-contrast imaging described by the dispersive real part β of φ in the off-resonant case.

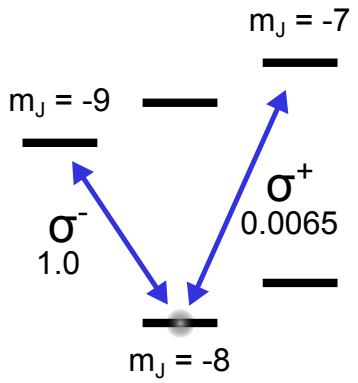

Figure 3.10.: Simplified level scheme of the 421 nm dipole transition between the $4f^{10}6s^2\ {}^5I_8$ ground state and the $4f^{10}({}^5I_8)6s6p({}^1P_1)\ (8,1)_9$ excited state in dysprosium. The relative transition strength is shown as well. The sample is fully spin-polarized in the lowest Zeeman sub-state ($m_J = -8$) of the ground state. Thus σ^- polarized light couples to the closed $m_J = -8 \leftrightarrow -9$ transition, while σ^+ light drives the $m_J = -8 \leftrightarrow -7$ transition. The latter is suppressed by a factor of ≈ 150 due to the difference in Clebsch-Gordan coefficients.

3.3.1. Absorption imaging

Absorption imaging is carried out with a σ^- polarized probe beam resonant to a closed transition. For dysprosium we use the strongest $\Delta J = 1$ transition at 421 nm which is a quasi-closed transition (depicted in fig. 3.10). The electric field ampltiude of the probe beam incident on the atoms is described by

$$\mathbf{E}_0 \equiv E_0\,\hat{\mathbf{e}}_- \quad \text{with} \quad \hat{\mathbf{e}}_- = \frac{1}{\sqrt{2}}\begin{pmatrix}1\\ -\mathrm{i}\end{pmatrix} \tag{3.30}$$

in the plane perpendicular to the propagation axis z described by Jones matrices [59]. As shown in eq. (3.28) the atomic sample introduces a phase shift of the electric field $\mathbf{E}_{\text{abs}} = e^{\mathrm{i}\varphi}\,\mathbf{E}_0$. The detected intensity on the camera is then given by

$$\frac{I_{\text{abs}}}{I_0} = \frac{\mathbf{E}_{\text{abs}}\mathbf{E}^*_{\text{abs}}}{E_0^2} = e^{-2\,\mathrm{Im}\{\varphi\}} \equiv e^{-OD} \tag{3.31}$$

with an exponential dependence on OD. This absorptive behavior of atoms on resonant light is also well described by the Beer-Lambert law [60]. In principle, this absorptive quantity is proportional to the scattering rate in eq. (3.2). However, the already shown calculations for $\alpha(\omega)$ in sec. 3.1 are only valid in the low-intensity and off-resonant limit. Hence, we use the quantum mechanical treatment which reveals a non-linear intensity dependence, the *power broadening* effect. Thereby, the optical density of a sample is given by

$$OD \equiv 2\,\mathrm{Im}\{\varphi\} = \tilde{n}(x,y)\underbrace{\frac{6\pi c^2}{\omega_0^2}}_{\sigma_0}\frac{1}{1+I/I_{\text{sat}}}\,, \tag{3.32}$$

where the saturation intensity is defined as $I_{\mathrm{sat}} = \frac{\hbar\Gamma\omega_0^3}{24\pi^2c^2}$ [39]. The optical peak absorption cross-section σ_0 directly relates the measured signal to the column density of atoms.
Experimentally such an image is taken with a CCD camera. Thus the acquired signal depends linearly on the light intensity I_{abs} with a certain detection efficiency A and an offset B. In order to extract the OD independently of the camera's properties we take three images. The first image $\tilde{I}_1$ is taken with atoms and therefore with the intensity distribution I_{abs} of eq. (3.31). The second one $\tilde{I}_2$ is taken without atoms ($OD = 0$), while the third one $\tilde{I}_3$ is taken without probe light ($I_0 = 0$):

$$\tilde{I}_1 = AI_{\mathrm{abs}} + B = AI_0e^{-OD} + B \qquad \tilde{I}_2 = AI_0 + B \qquad \tilde{I}_3 = B \tag{3.33}$$

From these three images we can extract the optical density

$$OD = \log\left(\frac{\tilde{I}_2 - \tilde{I}_3}{\tilde{I}_1 - \tilde{I}_3}\right), \tag{3.34}$$

which is independent of the camera characteristics A and B.
In general low-intensity absorption imaging ($I \ll I_{\mathrm{sat}}$) is limited to an OD on the order of 3 due to the limited dynamic range of CCD cameras[8]. This can be circumvented by using high intensities ($I > I_{\mathrm{sat}}$) to reduce the effective optical density in eq. (3.32) [61]. The downside is that more laser power is needed and only shorter laser pulses are allowed in order to avoid excessive heating of the sample.
We use absorption imaging to probe the density distribution of atoms after sufficiently long time-of-flight expansion, where the optical density is ≈ 1.

3.3.2. Phase-contrast imaging

To probe a dense sample like a BEC directly in the trap, where the optical density is an order of magnitude higher, a different approach is needed. *Phase-contrast polarization imaging* was first introduced in [40] and relies on the dispersive phase shift β instead of direct absorption giving rise to the optical density. Recalling eq. (3.7), the latter scales as $(\Gamma/\Delta)^2$ while β scales as (Γ/Δ). Thus we use an off-resonant beam ($\Delta = 18\,\Gamma$) to suppress absorption ($\mathrm{Im}\{\varphi\} \approx 0$). Therefore the phase shift $\varphi \approx \beta \ll 1$ in eq. (3.29) becomes small but purely dispersive [62].
In our setup the imaging axis is parallel to the magnetic field $\mathbf{B} \parallel \hat{\mathbf{e}}_z$. An incident electric field linearly polarized along the x axis

$$\mathbf{E}_0 \equiv E_0\,\hat{\mathbf{e}}_x = \frac{E_0}{\sqrt{2}}\,(\hat{\mathbf{e}}_+ + \hat{\mathbf{e}}_-) \quad \text{with} \quad \hat{\mathbf{e}}_\pm = \frac{1}{\sqrt{2}}\begin{pmatrix}1\\ \pm\mathrm{i}\end{pmatrix} \tag{3.35}$$

is thereby split into equal parts of σ^+ and σ^- polarized light described by Jones vectors $\hat{\mathbf{e}}_+$ and $\hat{\mathbf{e}}_-$. Therefore both corresponding transitions can be driven, as outlined in fig. 3.10.

[8] Typical dynamic resolution of a CCD camera is 12 or 14 bits, where a change of more than 3 orders of magnitude is often below the noise level.

The difference in resonance frequency due to Zeeman splitting is negligible for the chosen detuning. However, the σ^+ transition is a factor of ≈ 150 weaker compared to the closed σ^- transition due to a difference in Clebsch-Gordan coefficients. Effectively, atoms only couple to σ_- polarized light resulting in an electric field

$$\mathbf{E}_{\text{atoms}} = \frac{E_0}{\sqrt{2}} \left(\hat{\mathbf{e}}_+ + e^{\mathrm{i}\varphi}\, \hat{\mathbf{e}}_- \right) \overset{\varphi \approx \beta}{=} \frac{E_0}{\sqrt{2}} \left(\hat{\mathbf{e}}_+ + e^{\mathrm{i}\beta}\, \hat{\mathbf{e}}_- \right) . \tag{3.36}$$

Both coupled and uncoupled polarizations are combined on a linear polarizer transmitting with an angle θ to the initial linear polarization along x [59]. Thus the electric field vector

$$\mathbf{E}_{\text{pol}} = \begin{pmatrix} 1 & 0 \\ 0 & 0 \end{pmatrix} \begin{pmatrix} \cos\theta & \sin\theta \\ -\sin\theta & \cos\theta \end{pmatrix} \mathbf{E}_{\text{atoms}} = \frac{E_0}{2} \begin{pmatrix} (1 + e^{\mathrm{i}\beta})\cos\theta + \mathrm{i}(1 - e^{\mathrm{i}\beta})\sin\theta \\ 0 \end{pmatrix} \tag{3.37}$$

is reduced to one component along the polarizer's transmission axis. Due to interference of both polarizations the intensity

$$\begin{aligned} \frac{I_{\text{pol}}}{I_0} = \frac{\mathbf{E}_{\text{pol}} \mathbf{E}^*_{\text{pol}}}{E_0^2} = \cos^2\!\left(\theta - \frac{\beta}{2}\right) &\overset{\beta \ll 1}{\approx} \cos^2\theta + \frac{\beta}{2}\sin(2\theta) - \frac{\beta^2}{4}\cos(2\theta) \\ &= \begin{cases} \frac{1}{2}(1+\beta) & \text{for } \theta = 45^\circ \\ \frac{1}{4}\beta^2 & \text{for } \theta = 90^\circ \end{cases} \end{aligned} \tag{3.38}$$

depends on the dispersive phase shift β defined in eq. (3.29). Within the rotating wave approximation in eq. (3.7) it is given by

$$\beta = \frac{\omega}{2\varepsilon_0 c} \tilde{n}(x,y)\, \mathrm{Re}\{\alpha(\omega)\} \approx \frac{\sigma_0}{4} \tilde{n}(x,y) \left(\frac{\Gamma}{\Delta} \right) . \tag{3.39}$$

For an angle of $\theta = 90^\circ$ between the polarizer and the initial linear polarization the response is quadratic in β without a contribution by the uncoupled light field. This case is called *dark-field imaging* and has been used to nondestructively probe a BEC directly in the trap [63].
Since $\beta \ll 1$ the effect is relatively weak compared to the case for $\theta = 45^\circ$, where the relation between intensity and density of atoms is linear. This technique has been used for in-situ imaging of the first lithium BECs with less than 1000 atoms [40].
Here, we also take three images similar to the acquired images for absorption imaging, introduced in the previous section. To extract the optical density of the sample independently of the camera properties A and B we apply eq. (3.38 for $\theta = 45^\circ$) in the same manner:

$$\tilde{I}_1 = A I_{\text{pol}} + B = A \frac{1+\beta}{2} I_0 + B \qquad \tilde{I}_2 = A \frac{1}{2} I_0 + B \qquad \tilde{I}_3 = B \tag{3.40}$$

In this case the optical density is derived via

$$OD = 4\beta \left(\frac{\Delta}{\Gamma} \right) = 4\, \frac{\tilde{I}_1 - \tilde{I}_2}{\tilde{I}_2 - \tilde{I}_3} \left(\frac{\Delta}{\Gamma} \right) \tag{3.41}$$

which is proportional to detuning Δ. We use this approach for in-situ imaging of the trapped quantum gas in the high-resolution imaging setup described in the next section.

3.4. High-resolution imaging system

As mentioned in the preceding section we use a high-resolution imaging system to perform in-situ measurements of quantum gases. For example, the typical size of a BEC is on the order of some μm, see sec. 2.2.2. Thus we plan to use a setup with magnification $M = 50$ in the configuration shown in fig. 3.9. The two custom-made microscope objectives[9] we use are diffraction-limited and have focal lengths $f_1 = 25\,\text{mm}$ and $f_2 = Mf_1 = 1250\,\text{mm}$. Both are anti-reflection coated for the imaging wavelength $\lambda = 421\,\text{nm}$ as well as the EOD trapping light at 532 nm. Additionally, the first objective with small focal length features a high numerical aperture $NA = 0.32$ [64].
To obtain the resolution of such a system we can calculate the diffraction-limited spot size

$$d = \frac{1.22}{2}\frac{\lambda}{NA} = \frac{1.22}{2}\frac{421\,\text{nm}}{0.32} = 803\,\text{nm} \tag{3.42}$$

given by the Rayleigh criterion [59, 64]. Only the numerical aperture of the first objective is important here, because it limits the solid angle of collected light emitted from the imaged object.

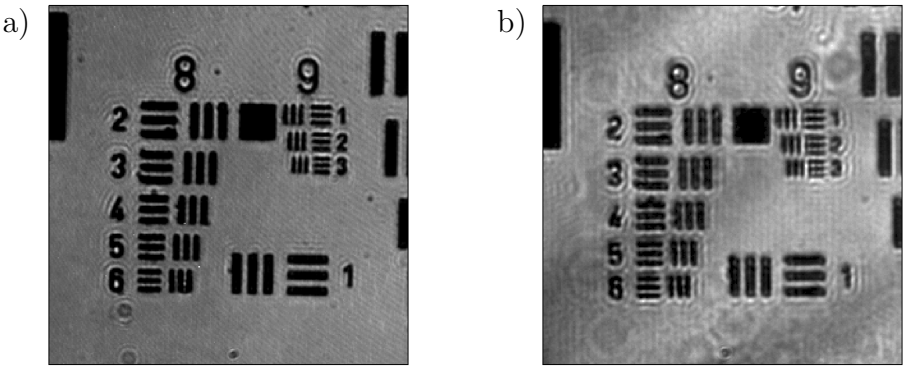

Figure 3.11.: Groups 8 & 9 of a *USAF resolution test chart*[10] imaged with a diffuse light source at $\lambda = 421\,\text{nm}$ (**a**) and 532 nm (**b**). In both cases the smallest horizontal & vertical bars (group 9, element 3) are visually distinguishable. This gives an upper limit of $1.56\,\mu$m for the resolution corresponding to twice the bar width of 780 nm [65].

Experimentally, the resolution of an optical system can be determined with the aid of a well-known test target, see fig. 3.11. The test target is illuminated with diffusive light at both wavelengths of interest and the imaging system together with the EMCCD camera is used to acquire an image. In this case we use a *USAF resolution test chart* with patterns of three bars with a certain width w separated by w. The resolution $2w$ is given by the minimum w where the three bars are still visually distinguishable. This is the case for all patterns at both wavelengths. The smallest pattern of group 9, element 3 with $w = 780\,\text{nm}$ [65] thus gives an upper limit to the resolution of $2w = 1.56\,\mu$m.

[9]Objectives: *Special Optics 54–17–25–532/421nm* and *54–17–1250–532/421nm*
[10]Target: *Edmund Optics 58–198* conforming to MIL–S–150A standard.

A more thorough approach is the usage of an approximate point source, in this case a pinhole with a diameter of 500 nm. Any optical system is characterized by its *point spread function* (PSF), the response to a perfect point source. For a cylindrally-symmetric system the PSF is an Airy function

$$A(r) = \left(\frac{2\, J_1(r)}{r} \right)^2 \tag{3.43}$$

with Bessel function of the first kind $J_1(r)$ [59]. In the Rayleigh criterion presented above the distance between $r = 0$ and the first zero-crossing at $r \approx 1.22\,\pi$ is defined as the resolution, motivating the numerical factor in eq. (3.42).

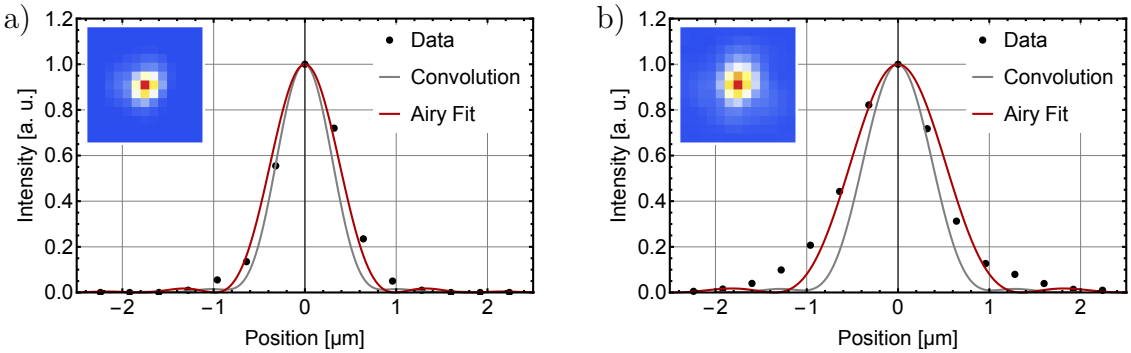

Figure 3.12.: Imaging a pinhole with 500 nm diameter for $\lambda = 421$ nm (**a**) and 532 nm (**b**). Black data points correspond to cuts through the inset images (pixel size of 0.32 μm). A gray line indicates the theoretical image given by the convolution of the objective's PSF and the object. A two-dimensional fit of the data to an Airy function (red) gives its zero-crossing $r_0 = (0.99 \pm 0.03)\,\mu$m and $r_0 = (1.36 \pm 0.05)\,\mu$m, respectively. According to the Rayleigh criterion, r_0 directly corresponds to the resolution.

As mentioned before, the theoretical imaging performance is mainly limited by the numerical aperture of the first objective. Thus we extract its PSF and convolute it with the object itself to obtain the theoretical diffraction-limited image of the object. This is shown in fig. 3.12 (gray) along with a cut (dots) through the experimentally acquired images (insets) and a fit (red) to an Airy function according to eq. (3.43). Although the convolution slightly changes the shape of the formerly Airy-shaped PSF we can use it to extract the resolution according to the Rayleigh criterion. For $\lambda = 421$ nm in fig. 3.12a the resolution is given by $r_0 = (0.99 \pm 0.03)\,\mu$m, which is close to the lower limit given by the convolution. In fig. 3.12b for $\lambda = 532$ nm the discrepancy to the convolution is higher and we find $r_0 = (1.36 \pm 0.05)\,\mu$m.
To conclude, the high-resolution imaging system is capable of acquiring images with micrometer resolution. For the EOD system a resolution of 1.36 μm is not a limiting factor because the waist diameter is calculated to be 2.2 μm, see eq. (3.23), and thus larger than the resolution. The whole imaging system is further characterized in a recent Bachelor thesis [64].

3.4.1. First in-situ images

The figures below show the performance of the high-resolution imaging system in the experiment. Fig. 3.13 presents one of our first phase-contrast images of a thermal clound at a temperature of roughly 400 nK.

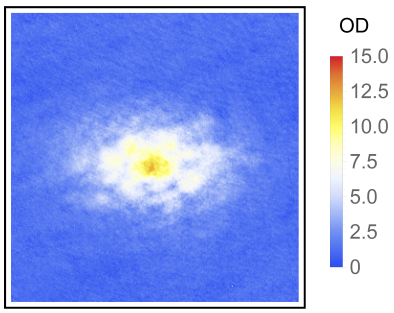

Figure 3.13.: In-situ image of a thermal cloud of atoms acquired via phase-contrast imaging. The detuning is $\Delta = 18\,\Gamma$ and the angle of the polarizer is $\theta = 45\,^\circ$. We use eq. (3.41) to extract the optical density. The field of view is $(96\,\mu\mathrm{m})^2$.

To align the objective we also use high-intensity resonant absorption imaging [61], which gives a much better signal-to-noise ratio. Yet, in order to extract the optical density we need to calibrate the intensity of the imaging light for future measurements. With this method we acquired our first in-situ image of a ^{164}Dy condensate, see fig. 3.14.

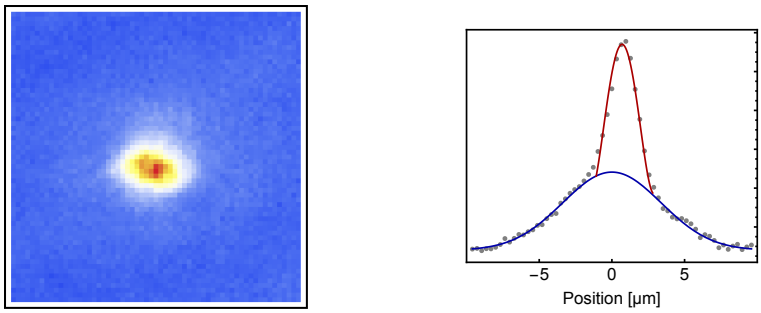

Figure 3.14.: In-situ image of a Bose-Einstein condensate acquired via high-intensity resonant absorption imaging. The horizontally integrated optical density (gray) follows a bimodal distribution with thermal (blue) and condensed atoms (red). According to eq. (3.32) the optical density depends on the intensity of the imaging light and thus needs to be calibrated in the future. Here, the field of view is $(19\,\mu\mathrm{m})^2$.

4. Bose-Einstein condensation of dysprosium

4.1. Magneto-optical trapping of dysprosium atoms

In order to cool a gas of atoms to quantum degeneracy several cooling steps are necessary. The initial laser cooling steps for dysprosium atoms have been thoroughly described in [31] and a diploma thesis [66]. The basics of laser cooling and magneto-optical trapping are explained in numerous textbooks, e.g. [39]. Thus we only give a short overview with some up-to-date values here.

The whole apparatus is shown in fig. 4.1. Starting at the bottom, dysprosium atoms are emitted from a high-temperature effusion cell at temperatures of $1200 - 1250\,^{\circ}\mathrm{C}$. For the Zeeman slower (ZS) and transversal cooling of the atomic beam we use the broad 421 nm transition with $\Gamma_{421} = 2\pi \cdot 32.2\,\mathrm{MHz}$ [67] and saturation intensity $I_{s,421} = \pi hc\Gamma/3\lambda^3 = 56.4\,\mathrm{mW/cm^2}$. The transversal cooling consists of two counter-propagating beams creating a two-dimensional optical molasses. The beams are red-detuned at $\Delta = -0.3\,\Gamma_{421}$ and elliptically shaped ($w_z = 6.8\,\mathrm{mm}$ and $w_r = 1.7\,\mathrm{mm}$ with respect to the atomic beam) to increase spatial overlap. The total power is typically $P_{\mathrm{trans}} = 200\,\mathrm{mW}$ leading to an intensity $I_{\mathrm{trans}} \approx 4.5\,I_{s,421}$ per beam. Under these conditions we typically gain a factor of 2.5 in MOT atom number with the optical molasses. After transversal cooling the atomic beam enters a spin-flip Zeeman slower. Its calculated capture velocity is 600 m/s, which allows us to capture $\approx 75\,\%$ of the intially Boltzmann-distributed atoms. The ZS beam is focused into the effusion cell with an estimated diameter of 18 mm at the MOT position. It has a power of $P_{\mathrm{ZS}} = 90\,\mathrm{mW}$ with a detuning $\Delta = -17.5\,\Gamma_{421}$ decreasing the velocity of atoms to $v \approx 10\,\mathrm{m/s}$.

Thereby atoms are slow enough to be captured by the MOT. Here we utilize the narrow 626 nm cycling transition with $\Gamma_{626} = 2\pi \cdot 136\,\mathrm{kHz}$ [68], $I_{s,626} = 72\,\mu\mathrm{W/cm^2}$ and a Doppler temperature of $T_{D,626} = \hbar\Gamma/2k_B = 3.3\,\mu\mathrm{K}$. The retro-reflected MOT beams have a diameter of 22.5 mm and an intensity of $I_{\mathrm{MOT}} \approx 240\,I_{s,626}$ per beam. At a detuning of $\Delta_{\mathrm{MOT}} = -34\,\Gamma_{626}$ and a magnetic field gradient of $\nabla B = 3\,\mathrm{G/cm}$ we typically load $110 \cdot 10^6$ atoms with a temperature on the order of $\approx 500\,\mu\mathrm{K}$ in 4 s into the MOT. The linewidth of the laser system in use is estimated to be $< 30\,\mathrm{kHz}$ [31]. Thus we use an electro-optical modulator (EOM) with a resonance frequency of 105 kHz to broaden the spectrum of the laser to a width of roughly $35\,\Gamma_{626}$. This results in an increased capture velocity of the MOT and thus in higher atom number at larger detuning, see fig. 4.2a.

In order to decrease the trapping volume and to reach colder temperatures we compress the

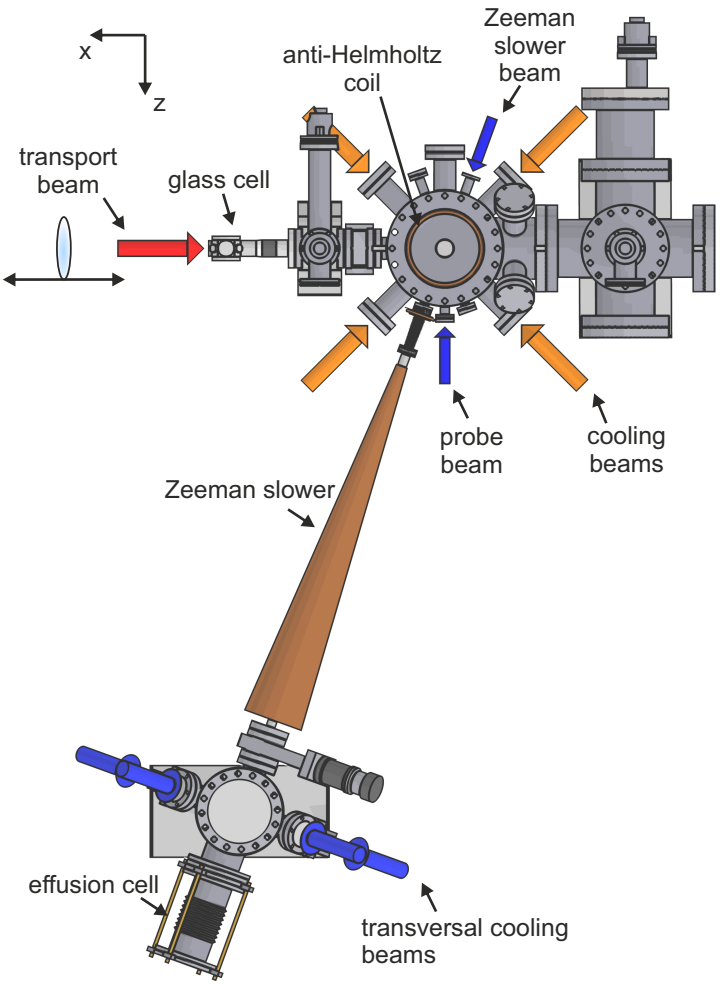

Figure 4.1.: Schematic view of the apparatus. Starting at the bottom, dysprosium atoms get emitted from an effusion cell. These are transversally cooled by four perpendicular beams and decelerated by a Zeeman slower (421 nm, blue arrows). At its end the narrow-line MOT operating at a wavelength of 626 nm (orange arrows) captures and subsequently cools the atoms to temperatures on the order of 10 μK. Then, atoms are loaded into an ODT (red arrow) and transferred to the glass cell on the left by moving the focusing lens (f = 1250 mm) of the ODT mounted on an air-bearing translation stage.

MOT after the loading stage in 170 ms by decreasing the intensity to $I_{\mathrm{MOT}} \approx 0.24\, I_{s,626}$, the detuning to $\Delta_{\mathrm{MOT}} = -5\,\Gamma_{626}$ and the magnetic field gradient to $\nabla B = 1.5\,\mathrm{G/cm}$. This procedure spatially compresses the atom cloud and lowers the final temperature to $12\,\mu\mathrm{K}$ allowing us to load the atoms directly in an optical dipole trap, as explained in the following chapter. It is worth noting that the atoms are optically pumped to the lowest Zeeman state $m_J = -8$ by the MOT [31]. With all atoms in the energetically lowest state inelastic collisions are suppressed at low temperature. Therefore no further repump lasers are needed at this stage.

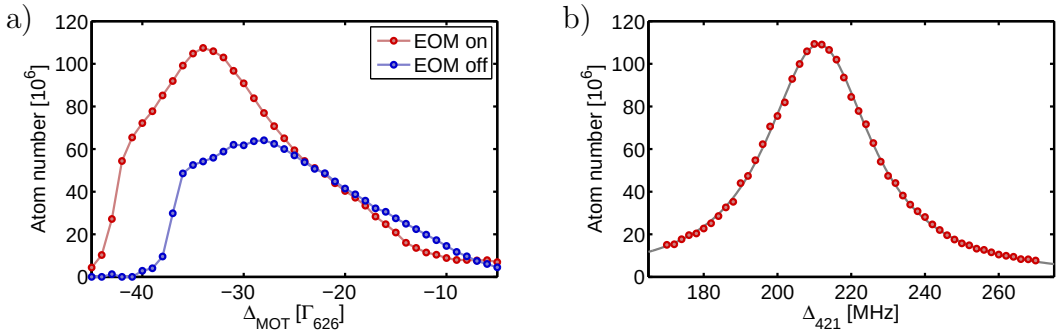

Figure 4.2.: (**a**) Atom number over detuning Δ_{MOT} of the 626 nm MOT beams with (red) and without (blue) the EOM used to broaden the laser spectrum. In (**b**) the atom number of the MOT is shown for different detunings Δ_{421} of the imaging light. The values are acquired by absorption imaging of the compressed MOT at $T \approx 12\,\mu\mathrm{K}$ after time-of-flight. A fit to a Voigt function gives a natural linewidth of $\Gamma_{421} = (33.0 \pm 1.0)\,\mathrm{MHz}$ for the Lorentzian convoluted with a Gaussian with width $\Sigma = (10.4 \pm 3.9)\,\mathrm{MHz}$ (both FWHM) broadening the observed spectrum.

Additionally, we employ the MOT to extract the linewidth of the 421 nm transition which is used for imaging. Hence we perform absorption imaging of the atom cloud and extract the number of atoms for varying detunings Δ_{421} of the imaging light. The acquired data is shown in fig. 4.2b with a fit according to a Voigt profile. The latter is a convolution of a Lorentzian given by the natural linewidth of the transition and a Gaussian due to inhomogenous broadening of the spectrum by the Doppler effect [39]. See [69, sec. 3.3] for the derivation of both lineshapes. Thereby we obtain the linewidth $\Gamma_{421} = (33.0 \pm 1.0)\,\mathrm{MHz}$ (FWHM) of the Lorentzian corresponding to the natural linewidth of the $\lambda = 421\,\mathrm{nm}$ transition. This value is in good agreement with $(32.2 \pm 0.8)\,\mathrm{MHz}$ acquired by spectroscopy of a thermal atomic beam [67].

4.2. Dysprosium atoms in an optical tweezer

In order to have better optical access we transfer the atoms with an optical tweezer from the MOT chamber to the science chamber, a glass cell. Fig. 4.3 illustrates the setup

used for optical trapping, further laser cooling and detection around the glass cell. In the following we give an overview of the different optical traps involved in the experiment.

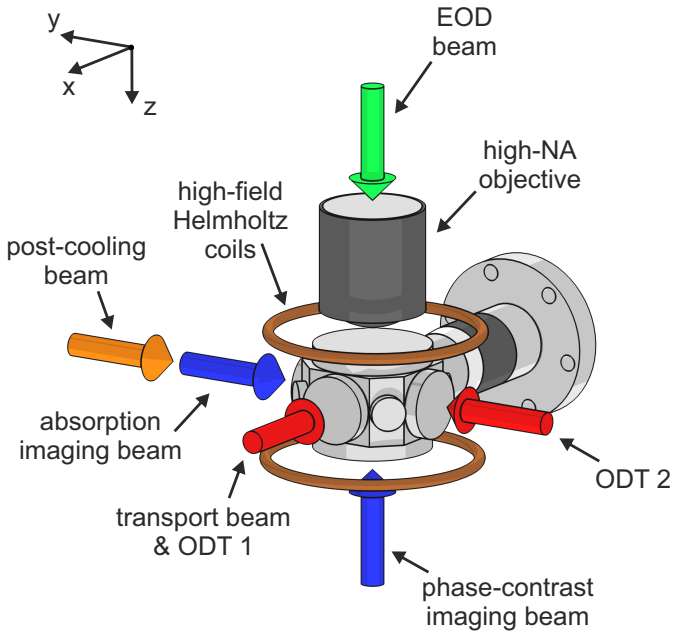

Figure 4.3.: Schematic view of the science chamber. The transport beam (red arrow) transfers the atoms from the MOT chamber to the glass cell. There, they are loaded into a crossed trap created by ODT 1 & 2. We also employ a laser cooling step with a beam red-detuned to the 626 nm transition (orange arrow). For time-of-flight measurements we use absorption imaging along the y direction (blue arrow). Phase-contrast imaging is performed for in-situ measurements in conjunction with the high-NA objective along z. The latter can also be used to write tailored potentials with the EOD system (green arrow). Close to the glass cell we also have a set of coils in Helmholtz configuration capable of generating magnetic fields up to 600 G.

Transport beam

For the optical transport we use a single-beam trap created by a broadband fiber laser[1] operating at 1070 nm. It has a measured beam waist of $w_0 = (37.3 \pm 1.2)\,\mu$m (see fig. 4.4a) and thus a Rayleigh length $z_R = 4.1$ mm. We further estimate the maximum beam power in the glass cell to 72 W. This laser cannot be used for evaporative cooling, because the frequency modes of the laser drive two-photon Raman transitions, see appendix A.2.

[1]Laser *IPG YLR-100-WP-WC*, $\lambda = 1070$ nm, $\Delta\lambda \approx 2$ nm, $P_{\max} = 100$ W.

ODT 1 & 2: Crossed trap for forced evaporation

Both traps are derived from a single-mode laser[2] operating at 1064 nm. Its beam is split into two paths for the two traps. The power of ODT 1 is controlled with a Pockels cell[3]. It is superimposed with the transport beam and has similar beam parameters to maximize the loading efficiency from the transport beam into ODT 1. The maximum power is $P = 28\,\mathrm{W}$ in the glass cell.
For ODT 2 we employ an AOM[4] and a high-power polarization-maintaining optical fiber. In order to reach the desired trap aspect ratio this beam is elliptical with waists $w_x = 150\,\mu\mathrm{m}$ and $w_z = 30\,\mu\mathrm{m}$. Here, the maximum power is $P = 8\,\mathrm{W}$.

EOD: Tailored intensity patterns

For the creation of tailored intensity patterns with the EOD system we use a 532 nm laser. The full setup has already been described in sec. 3.8.

4.2.1. Optical Transport

As mentioned in the previous section our narrow-line MOT produces a fully spin-polarized sample of $110 \cdot 10^6$ bosons in the lowest Zeeman state $m_J = -8$. At the end of the compression phase the $1/e^2$ radius of the cloud is about $400\,\mu\mathrm{m}$ at a temperature of $12\,\mu\mathrm{K}$. These are good starting conditions to load the atoms from the MOT in the transport beam. Recalling sec. 3.1.1 we can calculate the trap depth to

$$V_0 = \frac{\mathrm{Re}\{\alpha\}P}{\varepsilon_0 \pi c w_0^2} \approx 640\,\mu\mathrm{K} \tag{4.1}$$

with the polarizability $\mathrm{Re}\{\alpha\} = 102\,a.u.$ derived in the following section. There we also observe a decrease in trap frequencies for beam powers $> 40\,\mathrm{W}$ due to thermal lensing. This effect is taken into account here by increasing the waist size $w_0 = 37.3 \rightarrow 40.5\,\mu\mathrm{m}$, to match the trap frequencies at high power.
Thus the potential is deep enough to capture the atoms, yet the cloud of atoms is a factor of 10 larger at the end of MOT compression compared to the radial size of the beam. Therefore we do not load the dipole trap at the beam waist. Instead we employ the so-called "funnel" method, where the trap is loaded away from its trap minimum. During compression of the MOT we move the transport beam[5] and thus the trap minimum $\Delta x = 15\,\mathrm{mm} \approx 3z_R$ away from the MOT center. The waist size at this position is $w(\Delta x) \approx 170\,\mu\mathrm{m}$, which leads to an increase by a factor of $(170/40.5)^2 \approx 17.6$ in trapping

[2] Laser *Coherent Mephisto MOPA 55W*
[3] Pockels cell *Qioptiq DBBPC5*, intensity-stabilized in conjunction with a logarithmic photodiode and a PI controller (150 Hz bandwidth)
[4] AOM *AA Opto Electronic AA.MT.15*, 80 MHz, intensity-stabilized with a bandwidth of 4 kHz
[5] A $f = 1250\,\mathrm{mm}$ lens focuses the beam on the atoms. It is mounted on a computer-controlled air-bearing translation stage *Aerotech ABL15040* with 40 cm translation range and $0.5\,\mu\mathrm{m}$ accuracy.

area with the potential depth decreased by the same factor. We turn the transport beam on after the MOT compression phase and hold both traps for 120 ms, see fig. 4.4a for the beam profile of the transport beam. In the next step we release the atoms from the MOT by turning off its beams and the field gradient. Thus atoms are solely trapped in the transport beam and would oscillate in the trap, being released from an out-of-equilibrium position. To suppress sloshing of the sample we rapidly move the beam in 47 ms by $\Delta z = -15\,\mathrm{mm}$, so that the trap minimum is at the prior MOT position, indicated by the horizontal arrow in fig. 4.4a. The initial potential energy at the loading position heats up the sample to about $170\,\mu\mathrm{K}$. With this method we typically load $13 \cdot 10^6$ atoms into the transport beam. Yet, there are other methods to increase the loading efficiency. For example, an AOM can be used to increase the trapping volume of the ODT [70].

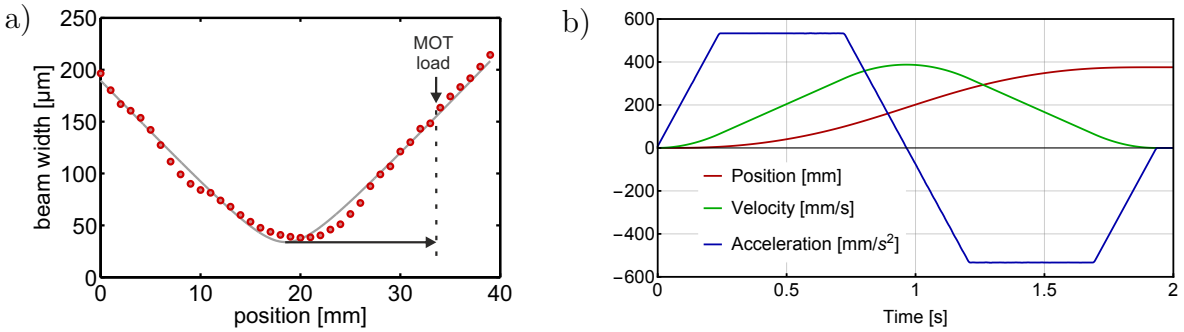

Figure 4.4.: (**a**) Beam width of the transport beam over its position. Data is extracted by Gaussian fits to images taken with a CCD camera. We obtain the beam waist $w_0 = (37.3 \pm 1.2)\,\mu\mathrm{m}$ with a fit to eq. (3.12). Arrows indicate the position of the MOT during loading and the subsequent movement of the focus to the MOT position. (**b**) Shows the position (red), velocity (green) and acceleration (blue) of the computer-controlled translation stage used for the optical transport.

Subsequently, we transfer the atoms from the MOT chamber over a range of 375 mm to the glass cell where the rest of the experiment is carried out. To avoid excessive heating of the sample we move the translation stage with the focusing lens of the transport beam in approx. 1.9 s as shown in fig. 4.4b . We choose a piecewise linear function (blue) for the acceleration. Thus the velocity is piecewise quadratic, while the position scales cubic. We typically obtain $N = 9 \cdot 10^6$ atoms at a temperature of $T = 120\,\mu\mathrm{K}$ in the glass cell. We measure the same values in the MOT chamber without moving the translation stage. Thus the optical transport is only limited by the lifetime of the atoms in the trap for the chosen parameters. For lower transport times we observe sloshing of the sample in the glass cell and for higher ones we get less atoms in the glass cell due to the limited lifetime.

After the transport stage we load the atoms from the transport beam in ODT 1. As mentioned both beams have similar beam parameters maximizing the spatial overlap and thus the loading efficiency, which is typically about 90 %.

4.2.2. Trap frequency & polarizability measurements

As motivated in chapter 2 the trap frequencies characterize the external harmonical potential. Therefore the knowledge of these is vital in order to describe the evaporation process and the condensate physics. In order to measure the trap frequencies we prepare a cloud of cold atoms at desired laser power and thus certain trap frequencies. We then employ one of the methods shown below to measure the trap frequencies.

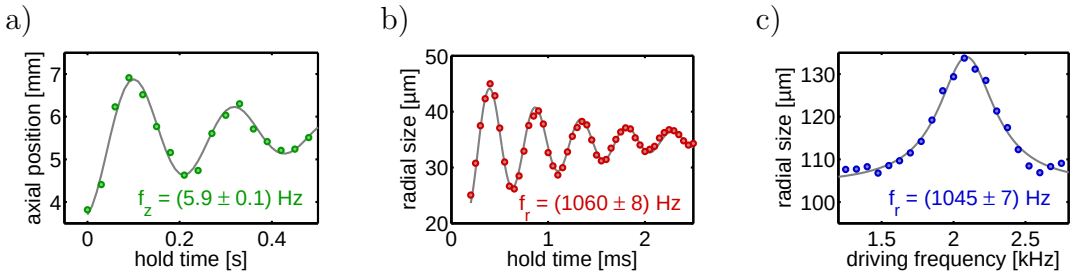

Figure 4.5.: Different methods to obtain the trap frequency. In (**a**) atoms are suddenly displaced along the optical axis z, thus they oscillate with trap frequency f_z. The "breathing mode" at twice the trap frequency can be driven by either turning the beam off for a time $t < 1/f$ (**b**) or by modulating the beam power at a certain frequency (**c**). For (a) & (b) an exponentially damped sine oscillation and for (c) a Lorentzian is fitted to the data taken with the transport beam at $P = 29.3\,\mathrm{W}$.

- **Displacement of the trap:** Monitoring the center-of-mass motion of an atom cloud in the trap is the most intuitive method to obtain the trap frequency. Thereby atoms are displaced from the equilibrium position and then released to oscillate. This can be accomplished with a gradient which is suddenly turned off [70]. With the translation stage we have another tool to displace the atoms along the axial direction in the transport beam. For this purpose the translation stage is suddenly displaced by half a Rayleigh length. Subsequently we observe a damped oscillation in the axial position at the axial trap frequency, see fig. 4.5a.

- **Blink:** Besides the fundamental mode we can also excite a breathing mode at twice the trap frequency. Thereby we turn the beam off for a time $t < 1/f$. The short release from the trap and subsequent recapture thus drives the center-of-mass oscillation along the gravitational axis. Furthermore the cloud is allowed to expand during the "blinking" time and subsequently recompressed driving the breathing mode. Fig. 4.5b shows the following damped oscillation in the cloud size suitable to measure the fast radial trap frequencies.

- **Driven oscillation:** We further use a parametric heating technique where we modulate the beam power at a driving frequency. This corresponds to a parametrically driven harmonic oscillator and energy is transferred to the cloud at harmonics of the trap frequency. Thus we observe a Lorentzian in the radial size corresponding

to an increased temperature, see fig. 4.5c. The highest transfer of energy to the sample occurs for the breathing mode at twice the trap frequency [60].

We employ the last two methods to extract the radial trap frequencies with relative uncertainties on the order of 1 %, see the fitted values in fig. 4.5b & c. In general the perturbation must be small in order to keep atoms in the quadratic region of the trap around the equilibrium position. For higher perturbations the oscillation frequencies of atoms in the trap become smaller and do depend on the amplitude of the perturbation [71].
The derivation of the trap frequencies for a single beam trap are shown in sec. 3.1.1. Here we combine eqs. (3.14) & (3.16) to obtain the radial trap frequency

$$f_r = \frac{1}{2\pi}\sqrt{\frac{4\,\mathrm{Re}\{\alpha\}}{\varepsilon_0\,\pi\,c\,m\,w_0^4}P} \tag{4.2}$$

for such a beam. Thus we can extract the real part of the polarizability $\mathrm{Re}\{\alpha\}$ by measuring the trap frequencies of the same beam at different beam powers P. In atomic physics this quantity is usually given in atomic units. The conversion factor for $\mathrm{Re}\{\alpha\}$ is $e^2a_0^2/E_h = 1.648777\cdot 10^{-41}\,\mathrm{C^2m^2J^{-1}}$ [72] defined by electron charge e, Bohr radius a_0 and Hartree energy E_h.

Polarizability for 1070 nm

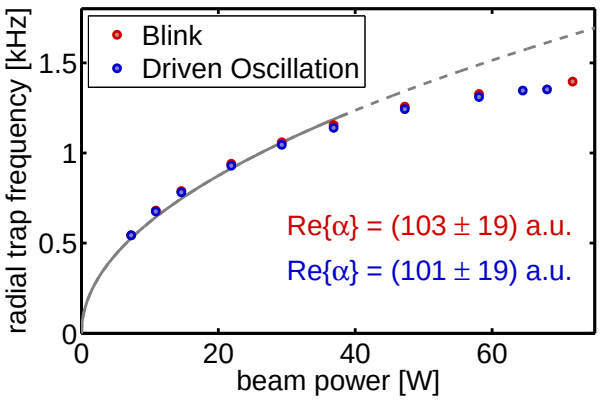

Figure 4.6.: Measurement of the radial trap frequency over the laser power of the transport beam. For the two methods shown here we observe excellent agreement. We extract the real part of the polarizability with a fit to eq. (4.2) for values up to 40 W. For higher power the trap frequencies are lower than expected due to thermal lensing. The error of the polarizability is mainly due to the error in the measurement of the beam waist $w_0 = (37.3 \pm 1.2)\,\mu$m.

For the broadband fiber laser at 1070 nm used for the optical transport we show the radial trap frequencies in fig. 4.6. In general the blinking method (red) and the data acquired by

modulating the beam power (blue) show excellent agreement. The relative errors of these measurements are less than 1 %, as already mentioned. With a fit (gray) of eq. (4.2) to the data up to a power of $P = 40\,\mathrm{W}$ we extract the respective polarizability. For higher laser power we observe a deviation from the $P^{1/2}$ power law due to thermal lensing. This is correlated with an increasing focal length of the last lens of the transport beam shifting the cloud of atoms axially. Thermal lensing thus occurs in prior components effectively reducing the beam size at the last lens and thus increasing the beam waist of the atoms. By fixing the extracted polarizability we can vary the beam waist $w_0 = 37.3 \rightarrow 40.5\,\mu\mathrm{m}$ in order to match the measured frequencies at full beam power.
Solving eq. (4.2) for $\mathrm{Re}\{\alpha\}$ we obtain a w_0^{-4} dependence. For the determination of the polarizability the accurate measurement of the beam waist is therefore critical. Hence an error of $17\,a.u.$ stems from the error of $1.2\,\mu\mathrm{m}$ in the beam waist measurement. The fit itself thus only contributes $2\,a.u.$ to the error. Combining both methods we get a value of $\mathrm{Re}\{\alpha\} = (102 \pm 20)\,a.u.$ for the atomic polarizability of ^{164}Dy at 1070 nm.

Polarizability for 1064 nm

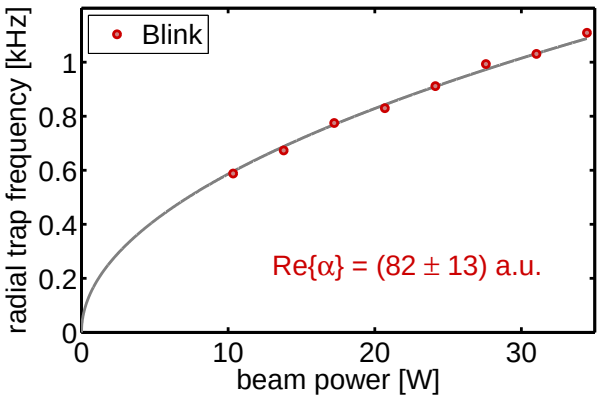

Figure 4.7.: Measurement of the radial trap frequency over the laser power of ODT 1. We extract the real part of the polarizability with a fit to eq. (4.2). The measured beam waist is $w_0 = (36.4 \pm 1.2)\,\mu\mathrm{m}$, the maximum power is 34.5 W.

In the same manner we measure the polarizability of atoms in ODT 1 operating at 1064 nm. Fig. 4.7 shows the data acquired with the "blinking" method as well as the fit to eq. (4.2) extracting $\mathrm{Re}\{\alpha\} = (82 \pm 13)\,a.u.$.
So far there are no precise measurements of the polarizability available. Only the Stanford group lists values of $116\,a.u.$ [67], updated to $75\,a.u.$ in [73] with comparable errors. In contrast theoretical calculations give larger values on the order of $180\,a.u.$ [74].

Polarizability for 532 nm

For 532 nm we only have a single measurement of the trap frequency in an early configuration with a green version of ODT 2. There we observe that the corresponding potential

is indeed attractive and thus $\mathrm{Re}\{\alpha\} > 0$. Solving eq. 4.2 for the polarizability we can give an estimate

$$\mathrm{Re}\{\alpha\} = \varepsilon_0 \, \pi \, c \, \frac{m w_0^4 \omega_r^2}{4P} \approx 10.5 \, a.u. \tag{4.3}$$

for a measured trap frequency of $\omega_r = 2\pi \cdot 275\,\mathrm{Hz}$, a beam power of $P = 8\,\mathrm{W}$ and a beam waist of $w_0 = 30\,\mu\mathrm{m}$.

4.2.3. Post-cooling with the 626 nm transition

After loading the atoms in ODT 1 where we have temperatures of around $30\,\mu\mathrm{K}$, we employ a laser cooling step. Thus we illuminate the atoms in the trap with a σ^- polarized beam (waist $w_0 = 3.0\,\mathrm{mm}$) along the y direction for 500 ms while we apply a $B = 2.3\,\mathrm{G}$ offset field in the same direction. Its frequency is red-detuned to the 626 nm cycling transition used for the MOT. The effects on atom number and temperature are shown in fig. 4.8 for different beam powers.

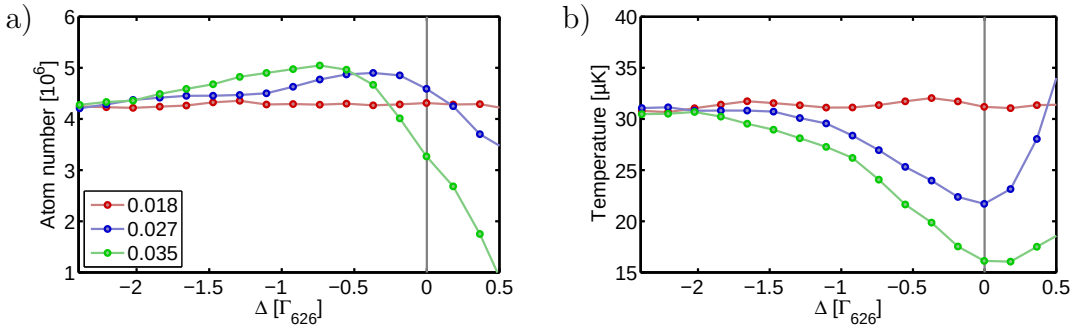

Figure 4.8.: Typical values of atom number (**a**) and temperature (**b**) over detuning for different saturation parameters $I/I_{s,626}$ of the red-detuned 626 nm post-cooling light. $\Delta = 0$ corresponds to the optimal detuning with the highest gain χ in phase-space density per atom loss, see eq. (4.6).

We compare the points of the actual power (green) with the reference points (red) for insufficient laser power. Thereby we can derive the efficiency of the cooling process according to eq. 4.6. We choose the optimal detuning (defined as $\Delta = 0$ here) where the cooling efficiency $\chi = 6.7$ is maximal. As seen in fig. 4.11 the efficiency for the forced evaporation ramps in the end of the cooling process is $\chi = 2.8$. For this efficiency the loss in atom number would be a factor of ≈ 1.4 higher compared to the laser cooling solution presented here.
A different and more promising approach is demagnetization cooling. The adiabatic demagnetization driven by inelastic dipolar collisions could be employed in conjunction with the optical pumping transition at 684 nm [32]. With this method a cooling efficiency $\chi > 11$ was observed in ^{52}Cr [75].

4.2.4. Forced evaporation to reach quantum degeneracy

The final cooling stages to reach quantum degeneracy utilize *forced evaporative cooling*. Fig. 4.9 shows the basic idea to remove the high-energy atoms from the thermal cloud in order to obtain a lower equilibrium temperature after thermalization. For optical traps the beam power P is continuously decreased. Thus the trap depth $V_0 \propto P$ decreases as well and atoms with energy $E > V_0$ are released from the trap. In order to increase the evaporation efficiency the change in trap depth $\partial V_0/\partial t$ should be as slow as possible [60, sec. 5.1]. On the other hand, atoms are subject to losses due to collisions with the background gas or three-body recombination limiting the lifetime of the atoms in the trap.

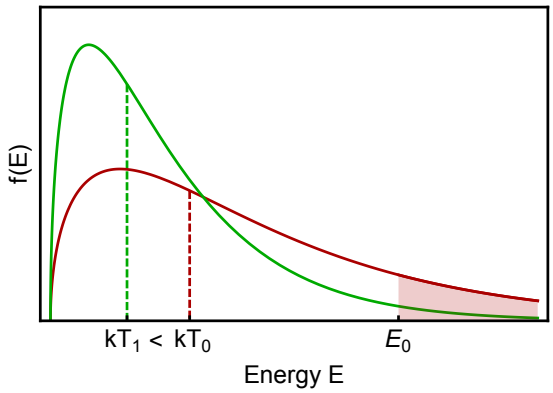

Figure 4.9.: Illustration of forced evaporation. The plot shows the Maxwell-Boltzmann distributed total particle energy E for initial temperature T_0 (red). Removing particles with energy $E > E_0$ (shaded region) results in a new equlibrium distribution (green) after thermalization due to elastic scattering. The temperature T_1 of the sample is lower as the initial temperature T_0. Thus it is cooled by removing the high energy particles.

The objective of the whole cooling process is to increase the phase-space density $\mathcal{D}$, defined in eq. (2.2), to values above unity. In a harmonic trap it is given by [60]

$$\mathcal{D} = n_0 \lambda_{dB}^3 = N \left(\frac{\hbar \bar{\omega}}{k_B T} \right)^3 \tag{4.4}$$

with the peak density of a thermal cloud

$$n_0 = N \bar{\omega}^3 \left(\frac{m}{2\pi k_B T} \right)^{3/2} \tag{4.5}$$

and the de Broglie wavelength according to eq. (2.3). To find the optimal timing for the forced evaporation process we define the *cooling efficiency*

$$\chi = -\frac{\log(\mathcal{D}_{k+1}/\mathcal{D}_k)}{\log(N_{k+1}/N_k)} \,. \tag{4.6}$$

It corresponds to the order of magnitude in phase-space density gain $\mathcal{D}_{k+1}/\mathcal{D}_k$ per order of magnitude in atom number loss N_{k+1}/N_k for the cooling step $k \to k+1$. Experimentally, we optimize the forced evaporation process by maximizing χ within the available parameter space of beam powers P_1 and P_2 of the crossed ODT and the time t for the linear ramps we choose.

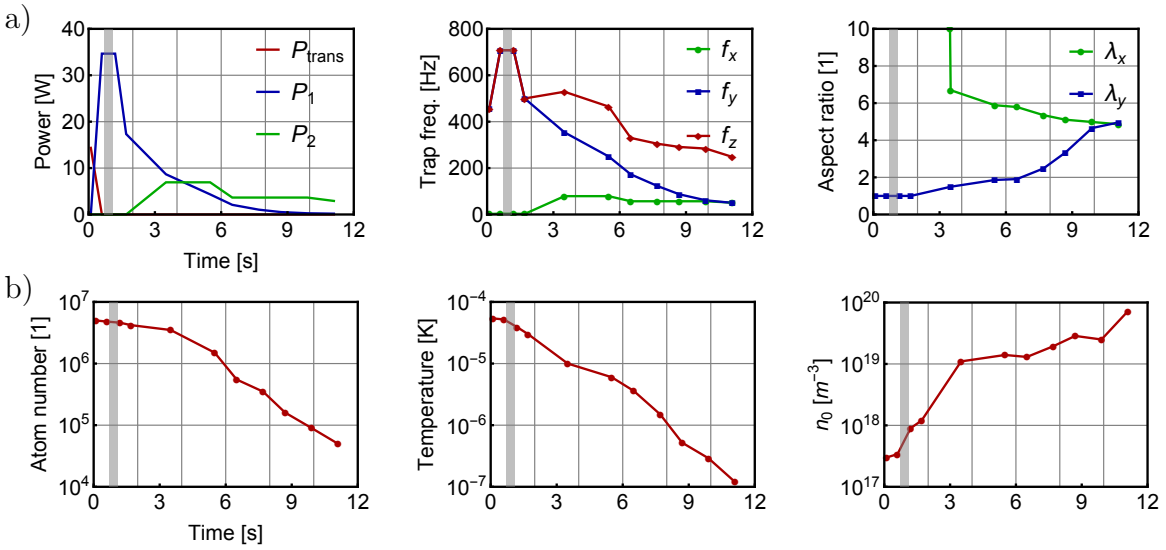

Figure 4.10.: Time evolution of the evaporation ramps. The shaded area indicates the post-cooling time of 500 ms. (**a**) Shows the laser power for the three ODTs as well as the calculated trap frequencies f_i and the trap aspect ratios λ_i perpendicular to the magnetic field axis $B \parallel z$. In the end we obtain a BEC in a radially symmetric trap with aspect ratio $\lambda = f_z/\sqrt{f_x f_y} = 5$. In (**b**) typical values for the total atom number, the temperature and peak density n_0 are presented.

Fig. 4.10 shows the experimental sequence in the glass cell along with typical values for atom number, temperature and peak density n_0. It starts with loading ODT 1 from the transport beam, followed by the laser cooling step (shaded area) described in the previous section. Subsequently we lower the power in ODT 1 while ramping up ODT 2 to increase the trap frequencies in x direction. In this crossed ODT we further lower the power for forced evaporative cooling. Finally, we have an oblate trap with trap aspect ratio $\lambda = f_z/\sqrt{f_x f_y} = 5$ with the atoms oriented along the magnetic field $B \parallel z$. The increase in peak density for the last evaporation step already indicates that the thermal cloud undergoes a phase transition to a condensate.
From the values in fig. 4.10b we can calculate the phase-space density according to eq. (4.4) as shown in fig. 4.11a. Within a double-logarithmic plot of $\mathcal{D}$ over the atom number N we analyze the cooling efficiency, see fig. 4.11b, for different cooling steps in the glass cell. χ is directly given by the slope in this plot, as indicated by the linear fit with $\chi = 2.8$ (gray) to the evaporation ramps in the crossed ODT. As mentioned in the last section, χ

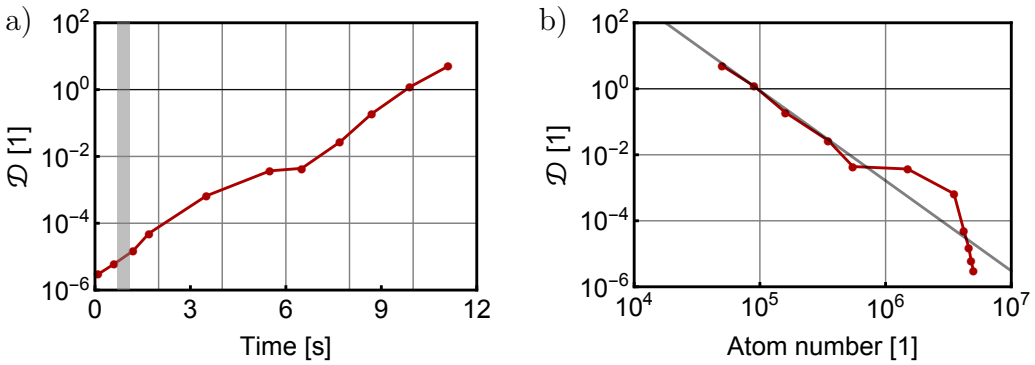

Figure 4.11.: Logarithmic plot of the phase-space density $\mathcal{D}$ over time (**a**) and atom number (**b**). The data is extracted from fig. 4.10 and calculated according to eq. 4.4. The slope χ in (**b**) corresponds to the gain in order of PSD per order of magnitude loss in atom number. Thus it is a measure for the efficiency of the evaporation process. A linear fit (gray) reveals $\chi = 2.8$ of the last evaporation ramps. In the beginning χ is higher for the post-cooling process and when turning on ODT 2.

is 6.7 for the laser cooling stage. We also observe a comparable efficiency when turning on ODT 2 due to an adiabatic transformation from the single beam trap with strong 2D confinement to a crossed ODT with strong confinement in all three directions, see [76] and [60, sec. 5.2.3].

4.3. Bose-Einstein condensation of Dysprosium

With the cooling methods shown in the previous sections we finally obtain a Bose-Einstein condensate of ^{164}Dy. In fig. 4.12c there are $N = 12{\cdot}10^3$ condensed atoms and $N_{th} = 84{\cdot}10^3$ remaining non-condensed atoms in the thermal cloud at a temperature of 130 nK. The condensate fraction is $N/(N + N_{th}) = 0.13$.
The final calculated trap frequencies after forced evaporation are $f_r = 50\,\text{Hz}$ and $f_z = 248\,\text{Hz}$. This corresponds to a mean trap frequency $\bar{\omega} = 2\pi \cdot 85\,\text{Hz}$ and a trap aspect ratio $\lambda = f_z/f_r = 5.0$ of the oblate trap.
The critical temperature for condensation is modified by the interactions and the finite-size of the condensate [38, 41]. Yet we can estimate it to $T_c \approx 180\,\text{nK}$ with eq. (2.6) for a non-interacting condensate.
Fig. 4.12 illustrates the phase transition to a BEC with absorption images (top) taken after a certain expansion time t_{tof}. Horizontal cuts (bottom) through the center show the underlying distribution of the optical density.
Above the critical temperature we obtain a Gaussian density distribution of the thermal cloud, see fig. 4.12a. Due to the long expansion time of 15 ms the extend of the cloud is mostly given by the Maxwell-Boltzmann distributed energy of the atoms. Thus it can

be utilized to extract the mean temperature of the thermal cloud [60], determined to $T = 290\,\mathrm{nK}$ here.

For lower temperatures close to the critical temperature T_c the classical Boltzmann-distribution shifts towards zero energy and we observe *Bose enhancement*. It corresponds to an augmented population of the lower states slightly increasing the density at the center compared to the previous case. The absorption image shown in fig. 4.12b is taken at $T = 160\,\mathrm{nK}$ just below the critical temperature where we observe the onset of condensation. Taking Bose enhancement into account we determine the number of condensed atoms to approximately 10^3.

Below T_c at $T = 130\,\mathrm{nK}$ we obtain a Bose-Einstein condensate of ^{164}Dy, see fig. 4.12c. The number of condensed atoms is $N = 12 \cdot 10^3$ with a condensate fraction of 0.13. The acquired density distribution is well described by a bimodal distribution with a Gaussian background of the thermal atoms and the quadratic behavior within the Thomas-Fermi approximation, see sec. 2.2.2.

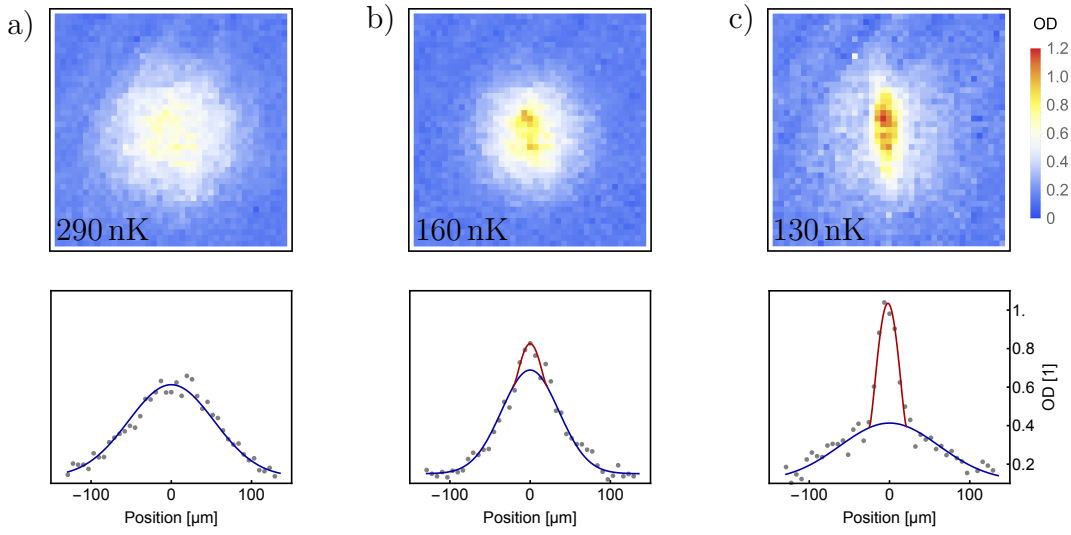

Figure 4.12.: Phase transition to a ^{164}Dy BEC. (**a**) shows a thermal cloud at a temperature of 290 nK. (**b**) For a lower temperature of 160 nK we observe the onset of the condensation. (**c**) Subsequently, we get a condensate of $N = 12 \cdot 10^3$ atoms. The non-condensed thermal atoms $N_{th} = 84 \cdot 10^3$ have a temperature of $T = 130\,\mathrm{nK}$ corresponding to a condensate fraction of 0.13. The absorption images (top) are taken after $t_{\mathrm{tof}} = 15\,\mathrm{ms}$ (a,b) and 20 ms (c) expansion time. We extract the temperature by a Gaussian fit to the wings of the distribution (blue). In (b) & (c) we fit a bimodal distribution with a column-integrated Thomas-Fermi parabola (red) [60, sec. 3.3.1] as shown in the plots of the horizontal cuts (bottom).

4.3.1. Stability of the BEC

More recently, we also observed Bose-Einstein condensation of ^{162}Dy. For this isotope we obtain condensate atom numbers of up to $N = 28 \cdot 10^3$ along with $N_{th} = 34 \cdot 10^3$ thermal atoms at a temperature of 70 nK, see fig. 4.13a. This corresponds to a condensate fraction of 0.45. Here we changed the trap geometry compared to the one in the previous section. In this crossed ODT the final trap frequencies $f_x = f_y = 42\,\mathrm{Hz}$ and $f_z = 143\,\mathrm{Hz}$ are lower. With a mean trap frequency $\bar{\omega} = 2\pi \cdot 63\,\mathrm{Hz}$ we calculate a critical temperature of $T_c = 130\,\mathrm{nK}$, see eq. 2.6. The trap is oblate with an aspect ratio $\lambda = f_z/\sqrt{f_x f_y} = 3.4$ and the condensate is thus stable according to the criterion derived in sec. 2.3.2.
Additionally, we also obtain ^{164}Dy condensates in the same trap for a similar cooling procedure. Yet for this isotope the final temperature is a factor of two higher, the condensate atom number about a factor of four lower. Thus we conclude that the efficiency of forced evaporative cooling is higher for ^{162}Dy. This indicates a larger elastic scattering cross section due to a higher scattering length a of ^{162}Dy compared to ^{164}Dy, as also pointed out in [28].

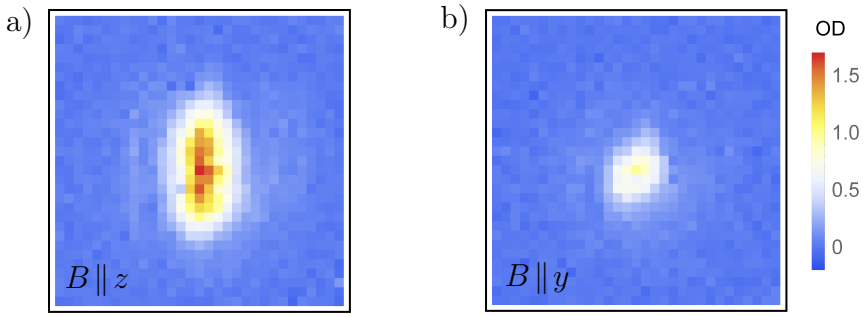

Figure 4.13.: (**a**) Shows an absorption image with $N = 28 \cdot 10^3$ condensed atoms of ^{162}Dy and a temperature $T = 70\,\mathrm{nK}$ of the thermal cloud with $N_{th} = 34 \cdot 10^3$ atoms. The magnetic field points along the trap symmetry axis $B \parallel z$. For this configuration the trap aspect ratio is $\lambda = f_z/\sqrt{f_x f_y} = 3.4$ and thus the BEC is stable. Under similar conditions but with a flipped magnetic field $B \parallel y$ the image in (**b**) is acquired. Here the effective trap aspect ratio $\lambda = f_y/\sqrt{f_x f_z} = 0.54$ is below the stability threshold and a BEC is not observed. Approximately $15 \cdot 10^3$ thermal atoms are left.

Finally, we study the stability of a dysprosium condensate. Thereby we can verify that the dipolar length a_{dd} is larger than the scattering length a and thus dysprosium is strongly dipolar. Recalling the stability criterion in fig. 2.6, a trap with $\lambda = f_z/\sqrt{f_x f_y} = 3.4 > 2$ stabilizes the condensate against collapse for up to 10^5 condensed atoms. Thus we get a condensate in fig. 4.13a with magnetic field $B \parallel z$. If we tilt the magnetic field B along the y direction, the effective trap aspect ratio along the new polarization axis changes to $\lambda = f_y/\sqrt{f_x f_z} = 0.54 < 2$. For a strongly dipolar BEC ($a_{dd} > a$) this region is only stable for condensate atom numbers up to approximately 2000. In agreement with this

prediction we do not observe a condensate for a magnetic field $B \parallel y$, see fig. 4.13b and [67]. Therefore we conclude that dysprosium is indeed strongly dipolar.

5. Conclusion & Outlook

In this thesis we have presented Bose-Einstein condensation of ^{162}Dy and ^{164}Dy. In order to describe such a condensate with contact and dipolar interaction we introduced the basic theoretical concepts as well as a stability criterion within the Gaussian approximation. Based on the latter we conclude that a dysprosium condensate is stable against a phonon-induced collapse in an oblate trap with aspect ratio $\lambda = \omega_z/\omega_r > 2$.
This calculation assumes an s-wave scattering length $a = 100\,a_0$, which has not been measured yet. In contrast the dipolar length $a_{dd} = 133\,a_0$ is well-defined by the atomic mass m and magnetic moment $\mu_m = 10\,\mu_B$. By flipping the magnetic field we investigated the stability of a ^{162}Dy condensate. This effectively transforms an oblate trap to a prolate one, where a strongly dipolar condensate is not stable. The absence of the latter indicates that the dipolar interaction is stronger than the contact interaction ($a_{dd} > a$) and thus $\varepsilon_{dd} = a_{dd}/a > 1$. In direct comparison ^{164}Dy shows inferior evaporative cooling efficiency indicating that its scattering length a is smaller. This suggests that the ε_{dd} parameter for ^{164}Dy is even larger.
We further showed the procedure to cool a thermal sample of dysprosium atoms emitted from an effusion cell to temperatures as low as 100 nK. This corresponds to ten orders of magnitude in temperature which we achieve with multiple laser cooling steps and subsequent forced evaporative cooling. For the former we employ a Zeeman slower at 421 nm as well as a magneto-optical trap at the narrow 626 nm transition. We directly load the atoms in an optical-dipole trap to transfer them over a range of 375 mm to the glass cell. There we employ laser cooling with a beam red-detuned to the 626 nm transition. Subsequently, we load the atoms in a crossed optical-dipole trap and perform forced evaporative cooling. This further increases the phase space density to finally obtain a Bose-Einstein condensate.
For the 421 nm transition we determine a linewidth of $\Gamma_{421}/2\pi = (33 \pm 1)$ MHz by extracting the atom number in the MOT for different detunings of the imaging beam.
By measuring the trap frequencies in the optical dipole traps for varying beam power we derived the dynamic polarizability $\mathrm{Re}\{\alpha\}$ of ^{164}Dy to $(102 \pm 20)\,a.u.$ at $\lambda = 1070$ nm and $(82 \pm 13)\,a.u.$ at 1064 nm. Additionally, we gave an estimate of $10.5\,a.u.$ at 532 nm.
Furthermore we have presented the first in-situ images acquired with the high-resolution imaging system. According to the Rayleigh criterion the resolution was measured to be $(0.99 \pm 0.03)\,\mu$m for 421 nm light. In conjunction with the electro-optical deflector system, which was also set up during this thesis, we plan to create tailored optical potentials with a 532 nm beam. At a planned waist diameter of $2.2\,\mu$m the measured resolution of $(1.36 \pm 0.05)\,\mu$m is not a limiting factor. By realizing multi-well and ring-shaped intensity

patterns we were also able to demonstrate the future capabilities of the deflector system.

Outlook

There are two possible improvements to increase the number of condensed atoms in the experiment. The critical temperature and thus the condensate fraction directly depend on the mean trap frequency, as seen in the first chapter. In optical traps the relation between trap depth and trap frequencies is fixed. Therefore either another trap configuration or a magnetic field gradient could be used to increase the mean trap frequency. The latter tilts the trapping potential via the Zeeman effect. This way the trap depth can be lowered while keeping the trap frequencies almost constant [77].
Increasing the cooling efficiency is another approach. As mentioned, demagnetization cooling has been successfully demonstrated in our group for chromium atoms with a cooling efficiency of $\chi > 11$ [75]. Light-assisted collisions limiting the efficiency can be further suppressed at certain detunings increasing the efficiency to values > 17 [78]. For dysprosium the recoil temperature, which is the lower limit for any laser cooling process, is lower because of the three times larger mass and a higher wavelength of the optical pumping transition. In fact, an estimation indicates that demagnetization cooling to quantum degeneracy should be possible in dysprosium [79].
By using the deflector system along with micrometer-resolution in-situ imaging we plan to investigate self-structured ground states in various tailored potentials. A possible starting point is a triple-well potential, where the long-range dipolar interaction alters the population of the single wells [48, 80]. These multi-well potentials are simple systems resembling primitive cells in solid state physics. Atoms in a ring-shaped potential are expected to mimic a self-induced bosonic Josephson junction [47]. With a magnetic field perpendicular to the symmetry axis of the ring potential atoms accumulate at two sites along the magnetic field axis creating a self-induced double-well potential due to the dipolar interaction. The system then shows oscillations in populations triggered by the initial population imbalance of the wells.
In fact the deflector system may also be used to generate artificial gauge fields by inducing direction-dependent tunneling between the wells of a multi-well pattern. This allows to simulate magnetism with neutral atoms. The underlying "time-periodic driving" method has been successfully applied to lattices [81, 82].
During writing this thesis, we also investigated the scattering properties of ^{164}Dy for different magnetic fields. We observed plenty of Feshbach resonances with a density of more than 4 per Gauss. The nearest neighbor distribution indicates a chaotic behavior similar to the one for erbium [83]. The results are shown in a future publication [84].

A. Appendix

A.1. Fermionic hyperfine structure

In contrast to the bosons the fermionic isotopes of dysprosium feature a finite nuclear magnetic moment $I = 5/2$ in addition to the total angular momentum $J = 8$. The coupling between these magnetic moments gives rise to the hyperfine structure of atomic energy levels introducing a new set of quantum numbers F and m_F [39]. While this is a good approximation for low magnetic fields the Zeeman effect becomes dominant at high magnetic fields and the coupling is negligible. Therefore the uncoupled basis $|J, m_J, I, m_I\rangle$ is used to calculate the energy shifts for arbitrary magnetic field B. The Hamiltonian [85]

$$H_{\text{hfs}} = A_{\text{hfs}}\boldsymbol{IJ} + B_{\text{hfs}}\frac{3(\boldsymbol{IJ})^2 + \frac{3}{2}\boldsymbol{IJ} - \boldsymbol{I}^2\boldsymbol{J}^2}{2I(2I-1)J(2J-1)} + \frac{\mu_B}{\hbar}(g_J J_z + g_I I_z)B \tag{A.1}$$

consists of coupling terms due to the magnetic dipole and electric quadrupole interaction as well as the Zeeman effect being proportional to the magnetic field B. The hyperfine structure constants A_{hfs} and B_{hfs} as well as the Landé factors g_J and g_I are specific to each state and have been determined experimentally [86].

To calculate the energy shift a vector of all possible states $|J, m_J, I, m_I\rangle \equiv |m_J, m_I\rangle$ is created. This vector spans a Hamiltonian matrix which is diagonalized numerically for each magnetic field B to obtain the eigenenergies. To calculate the non-zero matrix elements the product $\boldsymbol{IJ}$ is expressed in terms of the respective ladder operators as shown below in eq. (A.2 & A.3).

The energy shift of the ground state ${}^5I_8$ of both fermionic isotopes up to a magnetic field of 2000 G is calculated this way and shown in fig. (A.1). Interestingly the fine structure constant A_{hfs} of ^{161}Dy is negative. Therefore the spectrum is flipped compared to the one of ^{163}Dy for low magnetic fields.

$$
\begin{aligned}
& \boldsymbol{IJ}|m_J, m_I\rangle \\
= \quad & [I_x J_x + I_y J_y + I_z J_z] \ |m_J, m_I\rangle \\
= \quad & \left[\frac{1}{2} I_+ J_- + \frac{1}{2} I_- J_+ + I_z J_z\right] \ |m_J, m_I\rangle \\
= \quad & \frac{1}{2}\sqrt{(I - m_I)(I + m_I + 1)(J + m_J)(J - m_J + 1)}\, |m_J - 1, m_I + 1\rangle \\
+ \quad & \frac{1}{2}\sqrt{(I + m_I)(I - m_I + 1)(J - m_J)(J + m_J + 1)}\, |m_J + 1, m_I - 1\rangle \\
+ \quad & m_J m_I \, |m_J, m_I\rangle
\end{aligned}
\tag{A.2}
$$

$$
\begin{aligned}
& \left[3(\boldsymbol{IJ})^2 + \frac{3}{2}\boldsymbol{IJ} - \boldsymbol{I}^2\boldsymbol{J}^2\right] \ |m_J, m_I\rangle \\
= \quad & \frac{1}{2}\left[3m_I^2 - I(I+1)\right]\left[3m_J^2 - J(J+1)\right] \ |m_J, m_I\rangle \\
+ \quad & \frac{3}{4}(2m_I - 1)(2m_J + 1) \\
& \sqrt{(I + m_I)(I - m_I + 1)(J - m_J)(J + m_J + 1)}\, |m_J + 1, m_I - 1\rangle \\
+ \quad & \frac{3}{4}(2m_I + 1)(2m_J - 1) \\
& \sqrt{(I - m_I)(I + m_I + 1)(J + m_J)(J - m_J + 1)}\, |m_J - 1, m_I + 1\rangle \\
+ \quad & \frac{3}{4}\sqrt{(I + m_I)(I + m_I - 1)(I - m_I + 2)(I - m_I + 1)} \\
& \sqrt{(J + m_J + 2)(J + m_J + 1)(J - m_J)(J - m_J - 1)}\, |m_J + 2, m_I - 2\rangle \\
+ \quad & \frac{3}{4}\sqrt{(I + m_I + 2)(I + m_I + 1)(I - m_I)(I - m_I - 1)} \\
& \sqrt{(J + m_J)(J + m_J - 1)(J - m_J + 2)(J - m_J + 1)}\, |m_J - 2, m_I + 2\rangle
\end{aligned}
\tag{A.3}
$$

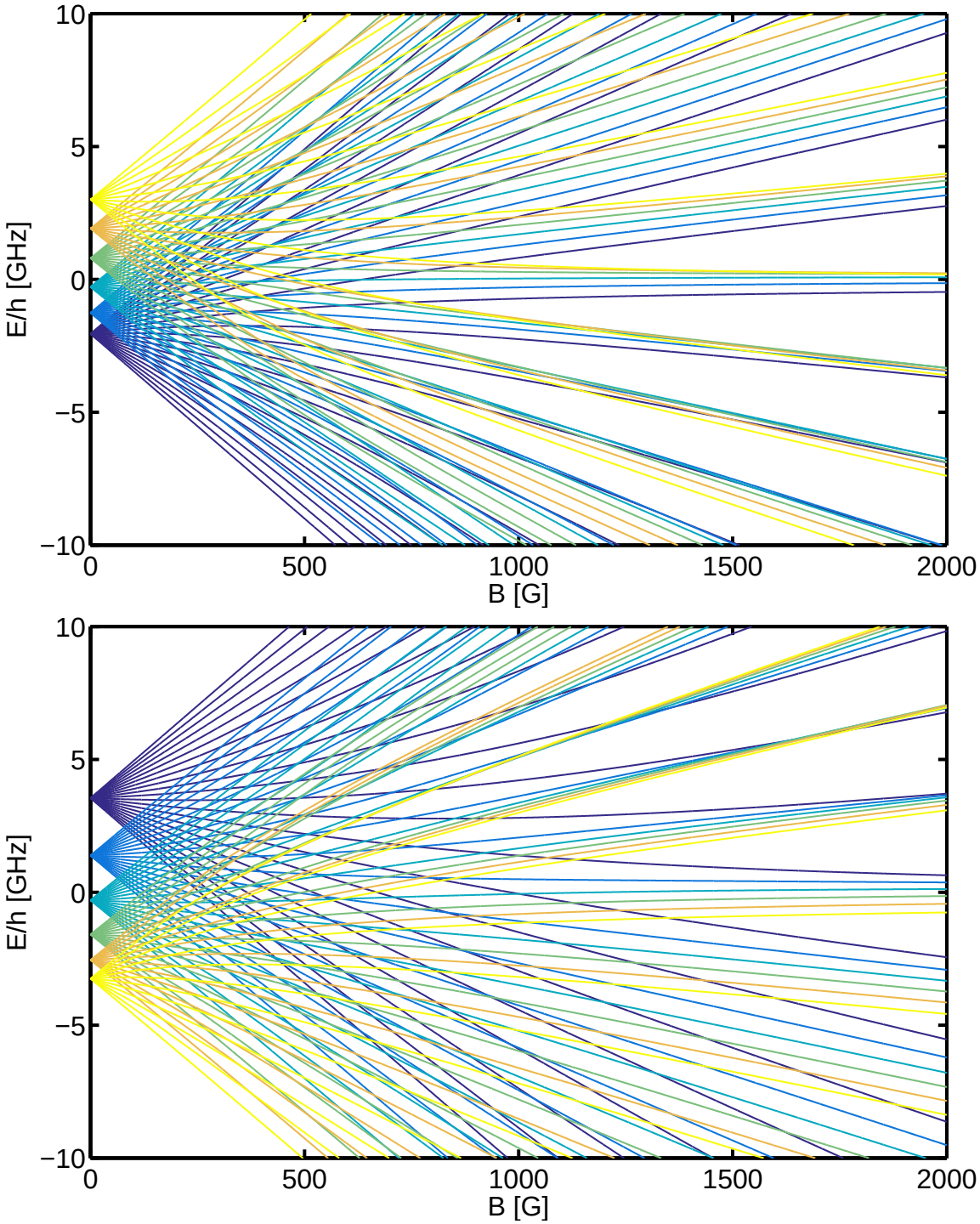

Figure A.1.: Hyperfine energy shift of the ground state of ^{161}Dy (top) and ^{163}Dy (bottom) as a function of magnetic field. Eigenenergies are colored by the low-field hyperfine quantum number $F = \frac{11}{2}$ (yellow), ..., $\frac{21}{2}$ (purple).

A.2. Mode spacing of the transport beam

The broadband fiber laser we use for the optical transport shows heating effects [87] which cannot be explained by the expected scattering rate of a far-detuned dipole trap, see chapter 3.

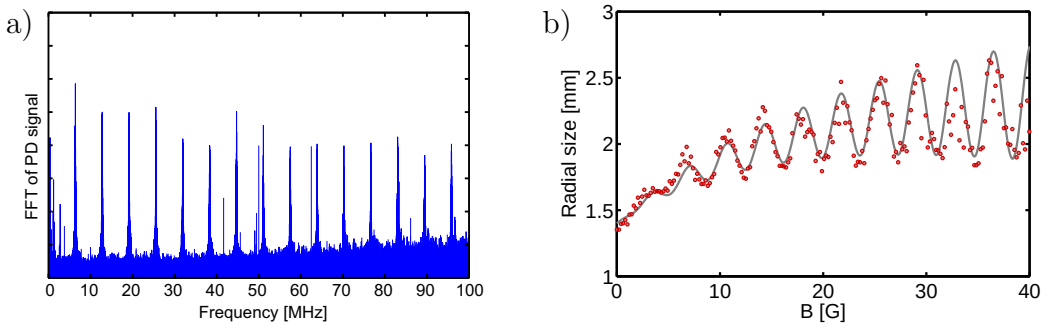

Figure A.2.: (**a**) Frequency spectrum of the transport beam recorded by a photodiode. Equidistant peaks with a spacing of $\approx 6.4\,\mathrm{MHz}$ are visible. (**b**) Radial size of a thermal cloud in the transport beam. The fit gives a period of $\Delta B = 3.7\,\mathrm{G}$ corresponding to a Zeeman splitting of $\Delta f = 6.43\,\mathrm{MHz}$. Data is extracted from absorption images taken after release from the trap and subsequent expansion.

An analysis of the laser spectrum in fig. A.2a shows equidistant lines with a frequency spacing of approx. 6.4 MHz corresponding to the mode spacing of the laser. Furthermore we observe induced heating and losses in atom number for certain magnetic fields in the experiment. Fig. A.2b shows the radial size of a cold thermal cloud imaged after time-of-flight for varying magnetic fields. There, the cloud size shows sinusoidal oscillations with a period of $\Delta B \approx 3.7\,\mathrm{G}$ corresponding to a Zeeman splitting $\Delta f = 6.43\,\mathrm{MHz}$ of the ground state. Maxima in size correspond to higher temperatures implying heating effects. The values are extracted by an artifical fit function of a cosine linearly increasing in amplitude and an exponentially saturating offset.
Therefore we conclude that the modes of the laser drive two-photon Raman transitions between the Zeeman levels of the ground state. This leads to induced heating when the Zeeman splitting is resonant to the mode spacing. Thereby it restricts the usage of the laser to certain magnetic fields inbetween these resonances. Thus we use a single-mode laser for the crossed optical dipole trap.

Bibliography

[1] R. P. Feynman, "Simulating physics with computers", Int J Theor Phys **21**, 467 (1982).

[2] I. Bloch, J. Dalibard, and W. Zwerger, "Many-body physics with ultracold gases", Rev. Mod. Phys. **80**, 885 (2008).

[3] C. Chin, R. Grimm, P. Julienne, and E. Tiesinga, "Feshbach resonances in ultracold gases", Rev. Mod. Phys. **82**, 1225 (2010).

[4] M. H. Anderson, J. R. Ensher, M. R. Matthews, C. E. Wieman, and E. A. Cornell, "Observation of Bose-Einstein condensation in a dilute atomic vapor", Science **269**, 198 (1995).

[5] K. B. Davis, M. O. Mewes, M. R. Andrews, N. J. van Druten, D. S. Durfee, D. M. Kurn, and W. Ketterle, "Bose-Einstein condensation in a gas of sodium atoms", Phys. Rev. Lett. **75**, 3969 (1995).

[6] C. C. Bradley, C. A. Sackett, J. J. Tollett, and R. G. Hulet, "Evidence of Bose-Einstein condensation in an atomic gas with attractive interactions", Phys. Rev. Lett. **75**, 1687 (1995).

[7] M. W. Zwierlein, J. R. Abo-Shaeer, A. Schirotzek, C. H. Schunck, and W. Ketterle, "Vortices and superfluidity in a strongly interacting Fermi gas", Nature **435**, 1047 (2005).

[8] J. Simon, W. S. Bakr, R. Ma, M. E. Tai, P. M. Preiss, and M. Greiner, "Quantum simulation of antiferromagnetic spin chains in an optical lattice", Nature **472**, 307 (2011).

[9] I. Bloch, J. Dalibard, and S. Nascimbène, "Quantum simulations with ultracold quantum gases", Nat Phys **8**, 267 (2012).

[10] T. Lahaye, C. Menotti, L. Santos, M. Lewenstein, and T. Pfau, "The physics of dipolar bosonic quantum gases", Rep. Prog. Phys. **72**, 126401 (2009).

[11] K. Góral, L. Santos, and M. Lewenstein, "Quantum phases of dipolar bosons in optical lattices", Phys. Rev. Lett. **88**, 170406 (2002).

[12] S. Yi, T. Li, and C. P. Sun, "Novel quantum phases of dipolar Bose gases in optical lattices", Phys. Rev. Lett. **98**, 260405 (2007).

[13] C. Menotti, C. Trefzger, and M. Lewenstein, "Metastable states of a gas of dipolar bosons in a 2D optical lattice", Phys. Rev. Lett. **98**, 235301 (2007).

[14] M. A. Baranov, K. Osterloh, and M. Lewenstein, "Fractional quantum Hall states in ultracold rapidly rotating dipolar Fermi gases", Phys. Rev. Lett. **94**, 070404 (2005).

[15] K. Osterloh, N. Barberán, and M. Lewenstein, "Strongly correlated states of ultracold rotating dipolar fermi gases", Phys. Rev. Lett. **99**, 160403 (2007).

[16] D. Peter, A. Griesmaier, T. Pfau, and H. P. Büchler, "Driving dipolar fermions into the quantum Hall regime by spin-flip induced insertion of angular momentum", Phys. Rev. Lett. **110**, 145303 (2013).

[17] B. M. Fregoso, K. Sun, E. Fradkin, and B. L. Lev, "Biaxial nematic phases in ultracold dipolar Fermi gases", New J. Phys. **11**, 103003 (2009).

[18] E. Fradkin, S. A. Kivelson, M. J. Lawler, J. P. Eisenstein, and A. P. Mackenzie, "Nematic Fermi fluids in condensed matter physics", Ann. Rev. of Condensed Matter Physics **1**, 153 (2010).

[19] R. A. Hart, P. M. Duarte, T.-L. Yang, X. Liu, T. Paiva, E. Khatami, R. T. Scalettar, N. Trivedi, D. A. Huse, and R. G. Hulet, "Observation of antiferromagnetic correlations in the Hubbard model with ultracold atoms", Nature **519**, 211 (2015).

[20] A. Griesmaier, J. Werner, S. Hensler, J. Stuhler, and T. Pfau, "Bose-Einstein condensation of chromium", Phys. Rev. Lett. **94**, 160401 (2005).

[21] A. Griesmaier, J. Stuhler, T. Koch, M. Fattori, T. Pfau, and S. Giovanazzi, "Comparing contact and dipolar interactions in a Bose-Einstein condensate", Phys. Rev. Lett. **97**, 250402 (2006).

[22] T. Lahaye, T. Koch, B. Fröhlich, M. Fattori, J. Metz, A. Griesmaier, S. Giovanazzi, and T. Pfau, "Strong dipolar effects in a quantum ferrofluid", Nature **448**, 672 (2007).

[23] T. Lahaye, J. Metz, B. Fröhlich, T. Koch, M. Meister, A. Griesmaier, T. Pfau, H. Saito, Y. Kawaguchi, and M. Ueda, "D-wave collapse and explosion of a dipolar Bose-Einstein condensate", Phys. Rev. Lett. **101**, 080401 (2008).

[24] T. Koch, T. Lahaye, J. Metz, B. Fröhlich, A. Griesmaier, and T. Pfau, "Stabilization of a purely dipolar quantum gas against collapse", Nat Phys **4**, 218 (2008).

[25] J. Werner, A. Griesmaier, S. Hensler, J. Stuhler, T. Pfau, A. Simoni, and E. Tiesinga, "Observation of Feshbach resonances in an ultracold gas of 52Cr", Phys. Rev. Lett. **94**, 183201 (2005).

[26] M. Lu, N. Q. Burdick, S. H. Youn, and B. L. Lev, "Strongly dipolar Bose-Einstein condensate of dysprosium", Phys. Rev. Lett. **107**, 190401 (2011).

[27] M. Lu, N. Q. Burdick, and B. L. Lev, "Quantum degenerate dipolar Fermi gas", Phys. Rev. Lett. **108**, 215301 (2012).

[28] Y. Tang, N. Q. Burdick, K. Baumann, and B. L. Lev, "Bose-Einstein condensation of 162Dy and 160Dy", arXiv (2014).

[29] K. Aikawa, A. Frisch, M. Mark, S. Baier, A. Rietzler, R. Grimm, and F. Ferlaino, "Bose-Einstein condensation of erbium", Phys. Rev. Lett. **108**, 210401 (2012).

[30] K. Aikawa, A. Frisch, M. Mark, S. Baier, R. Grimm, and F. Ferlaino, "Reaching Fermi degeneracy via universal dipolar scattering", Phys. Rev. Lett. **112**, 010404 (2014).

[31] T. Maier, H. Kadau, M. Schmitt, A. Griesmaier, and T. Pfau, "Narrow-line magneto-optical trap for dysprosium atoms", Opt. Lett. **39**, 3138 (2014).

[32] M. Schmitt, E. A. L. Henn, J. Billy, H. Kadau, T. Maier, A. Griesmaier, and T. Pfau, "Spectroscopy of a narrow-line optical pumping transition in atomic dysprosium", Opt. Lett. **38**, 637 (2013).

[33] S. N. Bose, "Plancks Gesetz und Lichtquantenhypothese", Z. Physik **26**, 178 (1924).

[34] A. Einstein, "Quantentheorie des einatomigen idealen Gases", (1925) 10.1007/BF01327326.

[35] L. P. Pitaevskii and S. Stringari, *Bose-Einstein condensation* (Clarendon Press, Apr. 3, 2003), 400 pp.

[36] W. Ketterle, "Superfluidity and coherence in Bose-Einstein condensates", Phys. Scr. **2002**, 36 (2002).

[37] C. J. Pethick and H. Smith, *Bose-Einstein condensation in dilute gases* (Cambridge University Press, 2002), 420 pp.

[38] F. Dalfovo, S. Giorgini, L. P. Pitaevskii, and S. Stringari, "Theory of Bose-Einstein condensation in trapped gases", Rev. Mod. Phys. **71**, 463 (1999).

[39] C. J. Foot, *Atomic physics* (Oxford University Press, 2005).

[40] C. C. Bradley, C. A. Sackett, and R. G. Hulet, "Bose-Einstein condensation of lithium: observation of limited condensate number", Phys. Rev. Lett. **78**, 985 (1997).

[41] K. Glaum, A. Pelster, H. Kleinert, and T. Pfau, "Critical temperature of weakly interacting dipolar condensates", Phys. Rev. Lett. **98**, 080407 (2007).

[42] K. Glaum and A. Pelster, "Bose-Einstein condensation temperature of dipolar gas in anisotropic harmonic trap", Phys. Rev. A **76**, 023604 (2007).

[43] H. Kadau, "A dipolar Bose-Einstein condensate in a one-dimensional optical lattice", Diploma Thesis (Universität Stuttgart, 5. Physikalisches Institut, Aug. 9, 2011).

[44] J. Stuhler, A. Griesmaier, T. Koch, M. Fattori, T. Pfau, S. Giovanazzi, P. Pedri, and L. Santos, "Observation of dipole-dipole interaction in a degenerate quantum gas", Phys. Rev. Lett. **95**, 150406 (2005).

[45] R. Grimm, M. Weidemüller, and Y. B. Ovchinnikov, "Optical dipole traps for neutral atoms", Advances in Atomic, Molecular and Optical Physics Vol. 42, 95-170 (2000).

[46] C. Cohen-Tannoudji and J. Dupont-Roc, *Atom-photon interactions: basic process and appilcations*, XXII (Wiley-VCH Verlag GmbH, 1998).

[47] M. Abad, M. Guilleumas, R. Mayol, M. Pi, and D. M. Jezek, "A dipolar self-induced bosonic Josephson junction", EPL **94**, 10004 (2011).

[48] D. Peter, K. Pawłowski, T. Pfau, and K. Rzażewski, "Mean-field description of dipolar bosons in triple-well potentials", J. Phys. B: At. Mol. Opt. Phys. **45**, 225302 (2012).

[49] R. Onofrio, D. S. Durfee, C. Raman, M. Köhl, C. E. Kuklewicz, and W. Ketterle, "Surface excitations of a Bose-Einstein condensate", Phys. Rev. Lett. **84**, 810 (2000).

[50] N. Friedman, A. Kaplan, D. Carasso, and N. Davidson, "Observation of chaotic and regular dynamics in atom-optics billiards", Phys. Rev. Lett. **86**, 1518 (2001).

[51] Y. Shin, M. Saba, T. A. Pasquini, W. Ketterle, D. E. Pritchard, and A. E. Leanhardt, "Atom interferometry with Bose-Einstein condensates in a double-well potential", Phys. Rev. Lett. **92**, 050405 (2004).

[52] V. J. Fowler and J. Schlafer, "A survey of laser beam deflection techniques", Applied Optics **5**, 1675 (1966).

[53] G. R. B. E. Römer and P. Bechtold, "Electro-optic and acousto-optic laser beam scanners", Physics Procedia, 8th International Conference on Laser Assisted Net Shape Engineering (LANE) **56**, 29 (2014).

[54] M. T. Valentine, N. R. Guydosh, B. Gutiérrez-Medina, A. N. Fehr, J. O. Andreasson, and S. M. Block, "Precision steering of an optical trap by electro-optic deflection", Opt. Lett. **33**, 599 (2008).

[55] C. Maurer, A. Jesacher, S. Bernet, and M. Ritsch-Marte, "What spatial light modulators can do for optical microscopy", Laser & Photon. Rev. **5**, 81 (2011).

[56] J. E. Curtis, B. A. Koss, and D. G. Grier, "Dynamic holographic optical tweezers", Optics Communications **207**, 169 (2002).

[57] G. D. Bruce, J. Mayoh, G. Smirne, L. Torralbo-Campo, and D. Cassettari, "A smooth, holographically generated ring trap for the investigation of superfluidity in ultracold atoms", Phys. Scr. **2011**, 014008 (2011).

[58] A. L. Gaunt and Z. Hadzibabic, "Robust digital holography for ultracold atom trapping", Sci. Rep. **2** (2012).

[59] B. E. A. Saleh and M. C. Teich, *Fundamentals of photonics* (Wiley, Feb. 5, 2013), 1202 pp.

[60] A. Griesmaier, "Dipole-dipole interaction in a degenerate quantum gas", PhD thesis (Universität Stuttgart, 5. Physikalisches Institut, July 14, 2006).

[61] G. Reinaudi, T. Lahaye, Z. Wang, and D. Guéry-Odelin, "Strong saturation absorption imaging of dense clouds of ultracold atoms", Opt. Lett. **32**, 3143 (2007).

[62] C. C. Bradley, "Bose-Einstein condensation of lithium", PhD thesis (Rice University, Dec. 1996).

[63] M. R. Andrews, M.-O. Mewes, N. J. v. Druten, D. S. Durfee, D. M. Kurn, and W. Ketterle, "Direct, nondestructive observation of a Bose condensate", Science **273**, 84 (1996).

[64] I. Reis, "Hochauflösendes Abbildungssystem für ultrakalte Atome", Bachelor Thesis (Universität Stuttgart, 5. Physikalisches Institut, Aug. 14, 2014).

[65] U. S. Military, *Military standard photograph lenses*, MIL-STD-150A (1951).

[66] M. Nickel, "Laser cooling of dysprosium atoms", Diploma Thesis (Universität Stuttgart, 5. Physikalisches Institut, Sept. 23, 2013).

[67] M. Lu, S. H. Youn, and B. L. Lev, "Spectroscopy of a narrow-line laser-cooling transition in atomic dysprosium", Phys. Rev. A **83**, 012510 (2011).

[68] M. Gustavsson, H. Lundberg, L. Nilsson, and S. Svanberg, "Lifetime measurements for excited states of rare-earth atoms using pulse modulation of a cw dye-laser beam", J. Opt. Soc. Am. **69**, 984 (1979).

[69] M. Schmitt, "High resolution laser spectroscopy of dysprosium", Master Thesis (Universität Stuttgart, 5. Physikalisches Institut, Oct. 23, 2012).

[70] S. Baier, "An optical dipole trap for erbium with tunable geometry", Master Thesis (Innsbruck, 2012).

[71] H. Gorniaczyk, "A crossed optical dipole trap", Diploma Thesis (Universität Stuttgart, 5. Physikalisches Institut, Dec. 15, 2011).

[72] P. J. Mohr, B. N. Taylor, and D. B. Newell, "CODATA recommended values of the fundamental physical constants: 2010", **41**, 043109 (2012).

[73] M. Lu, "Quantum Bose and Fermi gases of dysprosium: production and initial study", PhD thesis (Stanford University, Lev Group, May 2014).

[74] V. A. Dzuba, V. V. Flambaum, and B. L. Lev, "Dynamic polarizabilities and magic wavelengths for dysprosium", Phys. Rev. A **83**, 032502 (2011).

[75] M. Fattori, T. Koch, S. Goetz, A. Griesmaier, S. Hensler, J. Stuhler, and T. Pfau, "Demagnetization cooling of a gas", Nat Phys **2**, 765 (2006).

[76] P. W. H. Pinkse, A. Mosk, M. Weidemüller, M. W. Reynolds, T. W. Hijmans, and J. T. M. Walraven, "Adiabatically changing the phase-space density of a trapped Bose gas", Phys. Rev. Lett. **78**, 990 (1997).

[77] C.-L. Hung, X. Zhang, N. Gemelke, and C. Chin, "Accelerating evaporative cooling of atoms into Bose-Einstein condensation in optical traps", Phys. Rev. A **78**, 011604 (2008).

[78] J. Rührig, T. Bäuerle, A. Griesmaier, and T. Pfau, "High efficiency demagnetization cooling by suppression of light-assisted collisions", Opt. Express **23**, 5596 (2015).

[79] V. V. Volchkov, J. Rührig, T. Pfau, and A. Griesmaier, "Efficient demagnetization cooling of atoms and its limits", Phys. Rev. A **89**, 043417 (2014).

[80] B. Liu, L.-B. Fu, S.-P. Yang, and J. Liu, "Josephson oscillation and transition to self-trapping for Bose-Einstein condensates in a triple-well trap", Phys. Rev. A **75**, 033601 (2007).

[81] J. Struck, M. Weinberg, C. Ölschläger, P. Windpassinger, J. Simonet, K. Sengstock, R. Höppner, P. Hauke, A. Eckardt, M. Lewenstein, and L. Mathey, "Engineering Ising-XY spin-models in a triangular lattice using tunable artificial gauge fields", Nat Phys **9**, 738 (2013).

[82] P. Hauke, O. Tieleman, A. Celi, C. Ölschläger, J. Simonet, J. Struck, M. Weinberg, P. Windpassinger, K. Sengstock, M. Lewenstein, and A. Eckardt, "Non-abelian gauge fields and topological insulators in shaken optical lattices", Phys. Rev. Lett. **109**, 145301 (2012).

[83] A. Frisch, M. Mark, K. Aikawa, F. Ferlaino, J. L. Bohn, C. Makrides, A. Petrov, and S. Kotochigova, "Quantum chaos in ultracold collisions of gas-phase erbium atoms", Nature **507**, 475 (2014).

[84] T. Maier, *Emergence of chaotic scattering in ultracold Er and Dy* (manuscript in preparation, 2015).

[85] W. J. Childs, "Hyperfine structure of 5I8,7 atomic states of Dy161,163 and the ground-state nuclear moments", Phys. Rev. A **2**, 1692 (1970).

[86] J. Ferch, W. Dankwort, and H. Gebauer, "Hyperfine structure investigations in DyI with the atomic beam magnetic resonance method", Physics Letters A **49**, 287 (1974).

[87] T. Lauber, J. Küber, O. Wille, and G. Birkl, "Optimized Bose-Einstein-condensate production in a dipole trap based on a 1070-nm multifrequency laser: influence of enhanced two-body loss on the evaporation process", Phys. Rev. A **84**, 043641 (2011).

Danksagung

An dieser Stelle möchte ich einigen Leuten danken, die mich während des Studiums und vor allem der Durchführung dieser Arbeit begleitet haben.

- **Prof. Dr. Tilman Pfau** gilt mein besonderer Dank, da er mich bereits im fünften Semester für die Atomphysik begeistert hat und mir die Bachelor- und Masterarbeit am Institut ermöglichte.
- **Prof. Dr. Martin Dressel** in seiner Funktion als Mitberichter dieser Arbeit.
- **Thomas Maier**, **Holger Kadau** und **Matthias Schmitt**, den Urgesteinen im Düsi-Team, sowie **Isabel Reis**, **Igor Ferrier-Barbut** und **Clarissa Wink**, den "Neigschmeckten". Vielen Dank für die großartige Arbeitsatmosphäre, etliche Stunden im Labor und tausend kleine Dinge, die ich in diesem Jahr gelernt habe.
- Allen Mitarbeitern vom **5. Physikalischen Institut** für die unterhaltsamen Kaffeepausen, die vielen "mal kurz" ausgeliehenen Dinge und die Unterstützung mit allem was Verwaltung angeht.
- Zu guter letzt vielen Dank an **Lena**, **Christian**, **Philipp** und **Tobias** und vor allem an meine **Eltern**, die mich durch das Physik-Studium begleitet haben.